

# Non-Convex Tensor Low-Rank Approximation for Infrared Small Target Detection

Ting Liu, Jungang Yang, *Member, IEEE*, Boyang Li, Chao Xiao, Yang Sun, Yingqian Wang and Wei An

**Abstract**—Infrared small target detection plays an important role in many infrared systems. Recently, many infrared small target detection methods have been proposed, in which the low-rank model has been used as a powerful tool. However, most low-rank-based methods assign the same weights for different singular values, which will lead to inaccurate background estimation. Considering that different singular values have different importance and should be treated discriminatively, in this paper, we propose a non-convex tensor low-rank approximation (NTLA) method for infrared small target detection. In our method, NTLA adaptively assigns different weights to different singular values for accurate background estimation. Based on the proposed NTLA, we use the asymmetric spatial-temporal total variation (ASTTV) to thoroughly describe background feature, which can achieve good background estimation and detection in complex scenes. Compared with the traditional total variation approach, ASTTV exploits different smoothness strength for spatial and temporal regularization. We develop an efficient algorithm to find the optimal solution of the proposed model. Compared with some state-of-the-art methods, the proposed method achieve an improvement in different evaluation metrics. Extensive experiments on both synthetic and real data demonstrate the proposed method provide a more robust detection in complex situations with low false rates.

**Index Terms**—Infrared small target detection, non-convex tensor low-rank, asymmetric spatial-temporal total variation.

## I. INTRODUCTION

INFRARED small target detection is a key technique for many military applications, such as early-warning systems, maritime surveillance system, precision guided weapon and missile [1]–[3]. However, due to the long imaging distance of infrared detection systems, the targets always lack fixed shape or texture features. In addition, the targets are usually immersed in strong clutters and complex noises with low signal-to-clutter ratio (SCR). Therefore, research on infrared small target detection is of great significance and a challenging problem.

Infrared small target detection has been studied for decades, and various types of methods have been proposed. Among these methods, low-rank and sparse decomposition (LRSD) based methods are widely used because of its effectiveness. In infrared patch-tensor (IPT) model, sum of nuclear norm (SNN) [4] and tensor nuclear norm (TNN) [5] are usually introduced as the convex surrogate for tensor multi rank. However, the solution of SNN is actually suboptimal since

it transforms the tensor structure into three folding matrix along three dimension. Then, tensor nuclear norm (TNN) is proposed. Compared with SNN, TNN has better background estimation ability, but it assigns same weights for all singular values, which makes the model prone to false alarm and over-shrinkage problem. Further, the weighted nuclear norm minimization (WNNM) is introduced [6], [7]. However, WNNM can only alleviate the over-shrinkage problem to a certain extent. To further improve the accuracy of recovering background component, Sun et al. [8], [9] utilized weighted Schatten  $p$ -norm minimization (WSNM). More recently, Kong et al. [10] used nonconvex tensor fibered rank approximation for more accurate background estimation. In summary, how to obtain accurate background estimation is a crucial problem for infrared small target detection.

In this paper, we propose an infrared small target detection method via non-convex tensor low-rank approximation. Firstly, to approximate the rank function better than traditional nuclear norm, a non-convex surrogate via Laplace function has been proposed. The Laplace function can more tightly approximate to the  $l_0$  norm than  $l_1$  norm (see Fig.1). Meanwhile, it can adaptively assign weights to each singular value. Therefore, it is helpful to obtain more accurate background estimation. Additionally, considering that target is temporally consistent among successive frames and spatially smooth in local area. We exploit the ASTTV to thoroughly describe background feature, which can achieve good background detection in non-uniform and non-smooth scenes. Unlike TV which only considers spatial information and STTV which treats spatial TV and temporal TV operators equally, ASTTV upholds different smoothness strength for spatial TV and temporal TV, which helps to make better use of spatial-temporal information and is more flexible for target detection. Finally, asymmetric spatial-temporal total variation regularized non-convex tensor low-rank approximation for infrared small target detection is proposed, named the ASTTV-NTLA model. The pipeline of our proposed framework is illustrated in Fig. 2. The main contributions of this paper are summarized as follows.

(1) We propose a non-convex tensor low-rank approximation method for infrared small target detection. Different from existing low-rank methods, NTLA adaptively assigns different weights to different singular values through Laplace function, which helps to obtain an accurate background estimation.

(2) To capture both spatial and temporal information, the ASSTV regularization is incorporated into the LRSD method. This regularization can simultaneously preserve the spatial and temporal detail smoothness information. Therefore, it can achieve better performance in complex background scenarios.

This work was supported in part by the National Natural Science Foundation of China under Grant 61972435, Grant 61401474, and Grant 61921001. (Corresponding author: Jungang Yang)

T. Liu, J. Yang, B. Li, C. Xiao, Y. Sun, Y. Wang, and W. An are with the College of Electronic Science, National University of Defense Technology, Changsha, China. (e-mail: liuting@nudt.edu.cn, yangjungang@nudt.edu.cn).

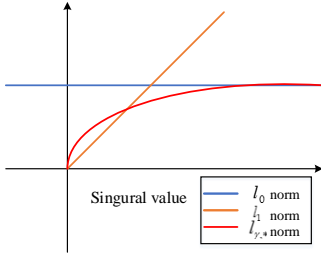


Figure 1. Comparison of the  $l_0$  norm,  $l_1$  norm, and  $l_{\gamma,*}$  norm for singular value

(3) We develop an efficient algorithm based on the ADMM to solve the ASTTV-NTLA. With the help of tensor singular value decomposition (t-SVD), the algorithm complexity and computation time are reduced, leading to a faster speed in comparison with similar methods.

The organization of the paper for the rest of sections appears in the following manner. Section II describes research work in related fields. We introduce some notations and preliminaries in Section III. In Section IV, the ASTTV-NTLA is proposed, and its optimization procedure is introduced. Section V presents the experimental results and performance evaluation along with discussion and analyses. Finally, we conclude this paper in Section VI.

## II. RELATED WORK

As mentioned above, according to the principle of algorithm, infrared small target detection methods can be divided into four categories. This section mainly describes these methods in detail.

### A. BS-based Infrared small Target Detection Methods

The BS-based methods treat the small target as a singular point that destroys the continuity of the local background area, such as 2D least mean square (TDLMS) filter [11], Top-Hat filter [12] and Max-Median filter [13], which first suppressed the background clutters and noise using the filter and then extract the small target with an intensity threshold. These methods obtain satisfactory computation efficiency. However, they will lead to high false alarm rates and poor detection performance under clutter, noise and other discontinuous backgrounds.

### B. HVS-based Infrared small Target Detection Methods

To better suppress the background clutters and noise while enhancing the small target, HVS [14]–[16] methods have been proposed. These methods suppose that the small target is more visually salient than its surrounding background. Based on the above ideas, Chen et al. [15] proposed a local contrast method (LCM) for infrared small target detection. Further, many improved LCM (ILCM) methods are proposed [16], such as multiscale relative LCM [17], weighted strengthened local contrast measure (WSLCM) [18], multiscale tri-layer local contrast measure (TLLCM) [19], and Gaussian scale-space enhanced LCM [20]. However, the performance of these methods would degrade for complex background cases that the

clutters are similar to the target in saliency maps. Moreover, the effectiveness of multi-scale filtering operation cannot be guaranteed.

### C. LRSD-based Infrared small Target Detection Methods

Another representative method is LRSD. This method is a branch of the popular low-rank representation (LRR) [21] in recent years. Gao et al. [22] first proposed a new infrared patch-image model (IPI) via local patch construction. Then the target-background separation problem is reformulated as a robust principal component analysis (RPCA) [23] problem. Subsequently, the LRSD methods were developed vigorously. However, due to the limitation of NNM, it will lead to over-shrinkage problem. To handle the above problems, Dai et al. [24] proposed the weighted infrared patch-image (WIPI) model via weighting each column in the patch image, but its computational complexity is relatively high. On this basis, Guo et al. [25] proposed a reweighted IPI (ReWIPI) model, in which WNNM was introduced to suppress sparse non-target pixels better. However, it can only alleviate the influence of over-shrinkage problem to a certain extent. Zhang et al. [26] exploited  $l_{2,1}$  norm to constrain clutter and proposed a non-convex rank approximation method (NRAM). Further, they proposed non-convex optimization with  $l_p$  norm constraint (NOLC) [27], which can better constrain sparse targets by  $l_p$  norm. To improve the robustness of the IPI model, some methods based on multi-subspace structure were designed, such as low-rank and sparse representation (LRSR) [28], stable multi-subspace learning methods (SMSL) [29] and self-regularized weighted sparse (SRWS) [30]. Encouraged by the powerfulness of TV regularization, Wang et al. [31] proposed a total variation regularization and principal component pursuit (TV-PCP) method.

Since the multiway tensor domain provides more views to dig out the inner relationship of the data than the matrix domain, a reweighted infrared patch-tensor (RIPT) method [4] is proposed, which extended the matrix domain to the tensor domain. However, due to the limitation of SNN, RIPT method achieves less competitive performance in complex scenes. To improve the performance of RIPT model, Sun et al. [6], [8] and Zhang et al. [5] exploited different tensor nuclear norms. Further, Kong et al. [10] proposed nonconvex tensor fibered rank approximation to infrared small target detection. In addition, to improve the robustness of RIPT model, Sun et al. [9] proposed a multiple subspace learning and spatial-temporal IPT (MSLSTIPT) method. Considering the importance of TV regularization, Sun et al. [7] proposed a spatial-temporal TV regularization and weighted IPT model (STTVWNIP), which extended the traditional TV to explore both the spatial and temporal information.

### D. DL-based Infrared small Target Detection Methods

Recently, deep learning based methods have attracted much attention due to its powerful feature learning ability. It is widely used in infrared small target detection [32]–[35]. Although they achieve improved performance, the main challenge of deep learning is that infrared small target lacks

remarkable texture and shape features, which makes feature learning difficult. In addition, the insufficient training set also limits its performance.

### III. NOTATIONS AND PRELIMINARIES

In this section, we introduce the basic notations and give detailed definitions related to the t-SVD scheme. In this paper, scalars, vectors, and matrices are denoted by lowercase letters (e.g.,  $x$ ); boldface lowercase letters (e.g.,  $\mathbf{x}$ ); and boldface capital letters (e.g.,  $\mathbf{X}$ ), respectively. Tensors are treated as multi-index arrays, which are denoted by Euler script (e.g.,  $\mathcal{X}$ ). Readers can refer to [36]–[40] for more details about TNN and t-SVD.

#### A. Adaptive Thresholding Using Laplace Function

To explore the low-rank nature of the background component, existing methods generally use the TNN. Moreover, t-SVD is performed by computing matrix SVDs of the frontal slices in the Fourier domain. For a tensor  $\mathcal{X} \in \mathbb{R}^{n_1 \times n_2 \times n_3}$ , the t-SVD [40] is given by

$$\mathcal{X} = \mathcal{U} * \Sigma * \mathcal{V}^T, \quad (1)$$

where  $\mathcal{U}$  and  $\mathcal{V}$  are orthogonal tensors of size  $n_1 \times n_1 \times n_3$  and  $n_2 \times n_2 \times n_3$ , respectively.  $*$  denotes the t-product, and  $\Sigma$  is the f-diagonal tensor of size  $n_1 \times n_2 \times n_3$ . Small singular values corresponds to noise or other sparse disturbances which can be removed by setting appropriate thresholds. Then, the remaining larger singular values can be used to reconstruct a low-rank tensor. The first step of t-SVD is to find the Fourier transform along the third dimension of  $\mathcal{X}$ . Suppose the result of the Fourier transform along the third dimension is  $\bar{\mathcal{X}}$ . Now, the multirank is a vector whose  $k^{th}$  component gives the rank of the  $k^{th}$  frontal slice, such as  $rank(\mathcal{X}) = (rank(\bar{X}_1), rank(\bar{X}_2), \dots, rank(\bar{X}_{n_3}))$ , where the  $k^{th}$  frontal slice is denoted as  $X^k$  [41], [42]. The sum of the singular values of all the frontal slices (i.e., TNN) is defined as

$$\|\mathcal{X}\|_* = \frac{1}{n_3} \sum_{k=1}^{n_3} \|\bar{X}_k\|. \quad (2)$$

TNN is considered as a surrogate of tensor multirank [43]. The disadvantage of TNN is that it assigns equal weight to all singular values of each frontal slice. However, for many natural images, the singular values have clear physical meanings and should be treated differently. Recently, the Laplace function is introduced into TNN to generate another non-convex approximation of tensor multi-rank [44], which can automatically assign the weight according to the importance of singular value. It is defined as follows:

$$\begin{aligned} \|\mathcal{X}\|_{\gamma,*} &= \sum_{k=1}^{n_3} \sum_i^{\min(n_1, n_2)} \phi(\sigma_i(\bar{X}_k)) \\ &= \sum_{k=1}^{n_3} \sum_i^{\min(n_1, n_2)} \phi\left(1 - e^{-\sigma_i(\bar{X}_k)/\varepsilon}\right), \end{aligned} \quad (3)$$

where  $\varepsilon$  is a positive constant and  $\sigma_i(\cdot)$  represents the  $i^{th}$  singular value.  $\phi(x) = 1 - e^{-x/\varepsilon}$  represents a Laplace function, which can better approximate to the  $l_0$  norm than the  $l_1$  norm

(see Fig.1). Therefore, the sum of the Laplace function is a better surrogate for tensor multi-rank. For  $\mathcal{Z}, \mathcal{Q} \in \mathbb{R}^{n_1 \times n_2 \times n_3}$ , let the globally optimal solution for the following problem

$$\arg \min_{\mathcal{Z}} \|\mathcal{Z}\|_{\gamma,*} + \frac{\eta}{2} \|\mathcal{Z} - \mathcal{Q}\|_F^2 \quad (4)$$

be  $\mathcal{Q} = \mathcal{U} * \Sigma * \mathcal{V}^H$ , where  $\mathcal{U}$  and  $\mathcal{V}$  are orthogonal tensors,  $*$  denotes t-product, and  $\Sigma$  is the f-diagonal singular value tensor. By performing the adaptive singular value thresholding to  $\mathcal{Z}$ , it can be written as

$$\bar{\mathcal{Z}} = \mathcal{U} * \mathcal{D}_{\frac{\nabla\phi}{\beta}} * \mathcal{V}^H, \quad (5)$$

where  $\mathcal{D}_{\frac{\nabla\phi}{\beta}} \in \mathbb{R}^{n_1 \times n_2 \times n_3}$  is an f-diagonal tensor whose each frontal slice in the Fourier domain is  $\bar{\mathcal{D}}_{\frac{\nabla\phi}{\beta}} \in \mathbb{R}^{n_1 \times n_2 \times n_3} = \left(\bar{S}(i, j, k) - \frac{\nabla\phi(\sigma_i^{k,l})}{\beta}\right)_+ \cdot \nabla\phi(\sigma_i^{k,l}) = \frac{1}{\varepsilon} \exp\left(-\frac{\sigma_i^{k,l}}{\varepsilon}\right)$  is the gradient of  $\phi$  at  $\sigma_i^{k,l}$ , and the  $i^{th}$  singular value of the  $k^{th}$  frontal slice of  $\Sigma$  at the  $l^{th}$  previous iteration. Each iteration solution of the optimization problem in Eq. (4) is briefly described in **Algorithm1**.

#### B. Asymmetric spatial-temporal total variation regularization

Total variation (TV) regularization is widely used in infrared small target detection, such as [31], [45], [46] because of its good performance in preserving the spatial piecewise smoothness, edge structure and spatial sparsity of the images. However, existing methods are based on matrix framework and can only describe the spatial continuity of small targets, but ignore their temporal continuity. Besides, the computation of SVD and TV regularization is time-consuming. Since target is temporally consistent among successive frames and spatially smooth in local area. Therefore, Sun et al. [8] extended the traditional TV to STTV, which explored both the spatial and temporal information. The remarkable performance of STTV-WNIPT demonstrate the effectiveness of simultaneously using spatial-temporal information. To model spatial and temporal continuity, we propose an asymmetric spatial-temporal total variation (ASTTV) regularization approach in the tensor framework [47]. It explores the spatial-temporal smoothness and temporal coherence of the small targets. There are two reasons for choosing the ASTTV regularization term. First, the regularization of smoothness on target for a smooth boundary and trajectory can be more efficiently achieved by imposing the ASTTV constraint [48]. Second, STTV-WNIPT enforces the spatial TV and temporal TV operators equally whereas ASTTV promotes different smoothness strength for spatial TV and temporal TV. Therefore, ASTTV is more flexible for target detection. The formulation of ASTTV regularization can be expressed as follows:

$$\|\mathcal{X}\|_{ASTTV} = \|D_h \mathcal{X}\|_1 + \|D_v \mathcal{X}\|_1 + \delta \|D_z \mathcal{X}\|_1, \quad (6)$$

where  $D_h$ ,  $D_v$  and  $D_z$  denote the horizontal, vertical and temporal difference operators, respectively, and  $\delta$  denotes a positive constant to control the contribution in temporal dimension. The ASTTV in Eq. (6) encourages both spatial and

temporal smoothness. The definitions of its three operators are expressed as

$$D_h \mathcal{X}(i, j, k) = \mathcal{X}(i+1, j, k) - \mathcal{X}(i, j, k) \quad (7)$$

$$D_v \mathcal{X}(i, j, k) = \mathcal{X}(i, j+1, k) - \mathcal{X}(i, j, k) \quad (8)$$

$$D_z \mathcal{X}(i, j, k) = \mathcal{X}(i, j, k+1) - \mathcal{X}(i, j, k). \quad (9)$$

---

**Algorithm1:** ADMM for solving the Eq. (4)

---

**Input:**  $\mathcal{X} \in \mathbb{R}^{n_1 \times n_2 \times n_3}$ ,  $\mathcal{Q}$ ,  $\eta$ ,  $\varepsilon$

**Output :**  $\bar{\mathcal{Z}}^{k+1}$ ,  $\mathcal{Z}^{k+1}$

**Step1:** Compute  $\bar{\mathcal{Q}} = \text{fft}(\mathcal{Q}, [], 3)$

**Step2** Compute each frontal slice of  $\bar{\mathcal{Z}}^{k+1}$  by  
**for**  $l = 1, \dots, [n_3 + 1/2]$  **do**

1.  $[\bar{\mathcal{U}}^l, \bar{\mathcal{S}}^l, \bar{\mathcal{V}}^l] = \text{SVD}(\bar{\mathcal{Q}}^l)$  ;

2. Compute  $\bar{D}_{\frac{\nabla \phi}{\eta}}^l$  by

$$\bar{D}_{\frac{\nabla \phi}{\eta}}^l = \left( \bar{\mathcal{S}}^l(i, j, k) - \frac{\nabla \phi(\sigma_i^{k,l})}{\eta} \right) +$$

3.  $(\bar{\mathcal{Z}}^{k+1})^l = \bar{\mathcal{U}}^l * \bar{D}_{\frac{\nabla \phi}{\eta}}^l * (\bar{\mathcal{V}}^l)^H$  ;

**end for**

**for**  $l = [n_3 + 1/2], \dots, 1$  **do**

$$(\bar{\mathcal{Z}}^{k+1})^l = \text{conj}((\bar{\mathcal{Z}}^{k+1})^{(n_3-l+2)})$$

**end for**

**Step3:** Compute  $(\mathcal{Z}^{k+1}) = \text{ifft}(\bar{\mathcal{Z}}^{k+1}, [], 3)$

---

#### IV. PROPOSED MODEL

##### A. Spatial-temporal Infrared Patch Tensor Model

Given an infrared image, it could be modeled as a linear superposition of target image, background image and noise image:

$$f_D = f_B + f_T + f_N, \quad (10)$$

where  $f_D$ ,  $f_B$ ,  $f_T$ , and  $f_N$  represent the input image, background image, target image, and noise image, respectively. we firstly use a sliding window from the top left to the bottom right over each image and stack all image patches from consecutive  $L$  frames into a 3D tensor. Similar to Eq. (10), we can divide the original tensor into three parts as below:

$$\mathcal{D} = \mathcal{B} + \mathcal{T} + \mathcal{N}, \quad (11)$$

where  $\mathcal{D}, \mathcal{B}, \mathcal{T}, \mathcal{N} \in \mathbb{R}^{n_1 \times n_2 \times n_3}$  are the original patch-tensor, background patch-tensor, target patch-tensor and noise patch-tensor, respectively.  $n_1$  and  $n_3$  denote the height and width of the sliding window, and  $n_2$  represents the number of the patches. Compared with the matrix-based methods, our data construction model has two advantages. Firstly, tensor domain provides more views to exploit the inner relationship of data. Secondly, the target detection performance is further improved by combining temporal information.

##### B. The proposed ASTTV-NTLA model

By integrating the non-convex tensor rank surrogate and ASTTV regularization into a unified framework, we propose a new model for infrared image small target detection:

$$\begin{aligned} \mathcal{B}, \mathcal{T}, \mathcal{N} = \arg \min_{\mathcal{B}, \mathcal{T}, \mathcal{N}} & \|\mathcal{B}\|_{\gamma,*} + \lambda_{tv} \|\mathcal{B}\|_{ASTTV} \\ & + \lambda_s \|\mathcal{T}\|_1 + \lambda_3 \|\mathcal{N}\|_F^2 \\ \text{s.t. } & \mathcal{D} = \mathcal{B} + \mathcal{T} + \mathcal{N}, \end{aligned} \quad (12)$$

where  $\|\cdot\|_{\gamma,*}$  is the Laplace function based TNN surrogate, and  $\lambda_{tv}$ ,  $\lambda_s$ ,  $\lambda_3$  denote the positive regularization parameters for ASTTV term, target and noise component, respectively. The first term  $\|\mathcal{B}\|_{\gamma,*}$  is used to separate the background from the whole infrared image. The second term  $\|\mathcal{B}\|_{ASTTV}$  is utilized to characterize the smooth structure of spatial-temporal domains to remove noise and enhance local detail information. The third term  $\|\mathcal{T}\|_1$  is used to find the sparse target. The last Frobenius norm term  $\|\mathcal{N}\|_F^2$  is further used to remove heavy noise. Then we can use Eq. (6) to rewrite Eq. (13) as below:

$$\begin{aligned} \mathcal{B}, \mathcal{T}, \mathcal{N} = \arg \min_{\mathcal{B}, \mathcal{T}, \mathcal{N}} & \|\mathcal{B}\|_{\gamma,*} + \lambda_s \|\mathcal{T}\|_1 + \lambda_3 \|\mathcal{N}\|_F^2 \\ & + \lambda_{tv} (\|\mathcal{D}_h(\mathcal{B})\|_1 + \|\mathcal{D}_v(\mathcal{B})\|_1 + \delta \|\mathcal{D}_z(\mathcal{B})\|_1) \\ \text{s.t. } & \mathcal{D} = \mathcal{B} + \mathcal{T} + \mathcal{N}, \end{aligned} \quad (13)$$

It is worth noting that the proposed model can fully capture the spatial and temporal information by incorporating the non-convex tensor low-rank surrogate and ASTTV regularization term. The main reasons is that the non-convex tensor rank surrogate ensures automatic weight assignment to the singular values. Furthermore, ASTTV is more flexible as compared with STTV for target detection.

##### C. Optimization Procedure

The optimization Eq. (13) can be solved effectively by using the ADMM [49] approach. By introducing four auxiliary variables  $\mathcal{Z}$ ,  $V_1 = \mathcal{D}_h(\mathcal{B})$ ,  $V_2 = \mathcal{D}_v(\mathcal{B})$ ,  $V_3 = \mathcal{D}_z(\mathcal{B})$ , we first rewrite the model from Eq. (13) into an equivalent function

$$\begin{aligned} \mathcal{B}, \mathcal{T}, \mathcal{N} = \arg \min_{\mathcal{B}, \mathcal{T}, \mathcal{N}} & \|\mathcal{Z}\|_{\gamma,*} + \lambda_s \|\mathcal{T}\|_1 + \lambda_3 \|\mathcal{N}\|_F^2 \\ & + \lambda_{tv} (\|V_1\|_1 + \|V_2\|_1 + \delta \|V_3\|_1) \\ \text{s.t. } & \mathcal{D} = \mathcal{B} + \mathcal{T} + \mathcal{N}, \mathcal{Z} = \mathcal{B}, V_1 = \mathcal{D}_h(\mathcal{B}), \\ & V_2 = \mathcal{D}_v(\mathcal{B}), V_3 = \mathcal{D}_z(\mathcal{B}). \end{aligned} \quad (14)$$

The inexact augmented Lagrangian multiplier (IALM) [50] approach is used to solve the Eq. (14), which is described as follows:

$$\begin{aligned} L_A(\mathcal{B}, \mathcal{T}, \mathcal{N}, \mathcal{Z}, V) & = \|\mathcal{Z}\|_{\gamma,*} + \lambda_s \|\mathcal{T}\|_1 + \lambda_{tv} (\|V_1\|_1 + \|V_2\|_1 + \delta \|V_3\|_1) \\ & + \langle y_1, \mathcal{D} - \mathcal{B} - \mathcal{T} - \mathcal{N} \rangle + \langle y_2, \mathcal{Z} - \mathcal{B} \rangle \\ & + \langle y_3, V_1 - \mathcal{D}_h(\mathcal{B}) \rangle + \langle y_4, V_2 - \mathcal{D}_v(\mathcal{B}) \rangle + \langle y_5, V_3 - \mathcal{D}_z(\mathcal{B}) \rangle \\ & + \frac{\mu}{2} (\|\mathcal{D} - \mathcal{B} - \mathcal{T} - \mathcal{N}\|_F^2 + \|\mathcal{Z} - \mathcal{B}\|_F^2 + \|V_1 - \mathcal{D}_h(\mathcal{B})\|_F^2 \\ & + \|V_2 - \mathcal{D}_v(\mathcal{B})\|_F^2 + \|V_3 - \mathcal{D}_z(\mathcal{B})\|_F^2) + \lambda_3 \|\mathcal{N}\|_F^2, \end{aligned} \quad (15)$$

where  $y_1, y_2, y_3, y_4, y_5$  represent the Lagrangian multiplier, and  $\mu$  is a positive penalty scalar. Applying ADMM can decompose the Eq. (15) into five optimization subproblems,



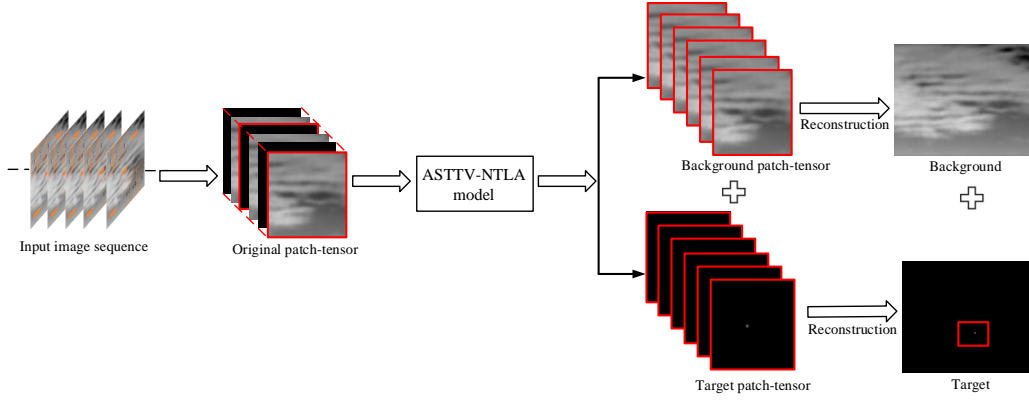


Figure 2. Overall framework of the proposed method.

including  $\mathcal{Z}$ ,  $\mathcal{B}$ ,  $\mathcal{T}$ ,  $V_1, V_2, V_3$ ,  $\mathcal{N}$ . Since it is hard to concurrently optimize all these variables, we approximately solve this optimization problem by alternately minimizing one variable with the others being fixed. The details are given as follows:

1) Updating  $\mathcal{Z}$  with other variables being fixed:

$$\mathcal{Z}^{k+1} = \arg \min_{\mathcal{Z}} \left\| \mathcal{Z} \right\|_{\gamma,*} + \frac{\mu^k}{2} \left\| \mathcal{Z} - \mathcal{B}^k + \frac{y_2^k}{\mu^k} \right\|_F^2. \quad (16)$$

Let  $\mathcal{B}^k - \frac{y_2^k}{\mu^k} = \mathcal{U} * \mathcal{S} * \mathcal{V}^H$ , then the optimal solution can be obtained by (5). Thus, the solution of (16) is

$$\mathcal{Z}^{k+1} = \mathcal{U} * \mathcal{D}_{\frac{\nabla \phi}{\beta}} * \mathcal{V}^H, \quad (17)$$

where  $\mathcal{D}_{\frac{\nabla \phi}{\beta}} = \left( \bar{S}(i, j, k) - \frac{\nabla \phi(\sigma_i^{k,l})}{\beta} \right)_+$ . The detailed solving process of Eq. (16) is shown in **Algorithm 1**.

2) Updating  $\mathcal{B}$  with other variables being fixed:

$$\mathcal{B}^{k+1} = \frac{\mu^k}{2} \left( \left\| \mathcal{D} - \mathcal{B} - \mathcal{T}^k - \mathcal{N}^k + \frac{y_1^k}{\mu^k} \right\|_F^2 + \left\| \mathcal{Z}^{k+1} - \mathcal{B} + \frac{y_2^k}{\mu^k} \right\|_F^2 + \left\| V_1^k - D_h \mathcal{B} + \frac{y_3^k}{\mu^k} \right\|_F^2 + \left\| V_2^k - D_v \mathcal{B} + \frac{y_4^k}{\mu^k} \right\|_F^2 + \left\| V_3^k - D_z \mathcal{B} + \frac{y_5^k}{\mu^k} \right\|_F^2 \right). \quad (18)$$

The solution to Eq. (18) is equivalent to the following liner system of equations:

$$(2\mathbf{I} + \Delta) \mathcal{B}^{k+1} = L^k + \theta_1 + \theta_2 + \theta_3, \quad (19)$$

where  $\Delta = D_h^T D_h + D_v^T D_v + D_z^T D_z$ ,  $L^k = \mathcal{D} - \mathcal{T}^k - \mathcal{N}^k + \frac{y_1^k}{\mu^k} + \mathcal{Z} + \frac{y_2^k}{\mu^k}$ ,  $\theta_1 = D_h^T \left( V_1^k + \frac{y_3^k}{\mu^k} \right)$ ,  $\theta_2 = D_v^T \left( V_2^k + \frac{y_4^k}{\mu^k} \right)$ ,  $\theta_3 = D_z^T \left( V_3^k + \frac{y_5^k}{\mu^k} \right)$ , and  $\mathbf{T}$  is the matrix transpose. By considering  $D_h \mathcal{B}$ ,  $D_v \mathcal{B}$ , and  $D_z \mathcal{B}$  as convolutions along two spatial directions and one temporal direction, this problem has a closed form solution via nFFT.

$$\mathcal{B}^{k+1} = \mathcal{F}^{-1} \left( \frac{\mathcal{F} \left( L^k + \theta_1 + \theta_2 + \theta_3 \right)}{2 + \sum_{i \in \{h, v, z\}} \mathcal{F}(D_i)^H \mathcal{F}(D_i)} \right), \quad (20)$$

where  $\mathcal{F}$  is the fast nFFT operator,  $\mathcal{F}^{-1}$  is the inverse nFFT operator, and  $\mathbf{H}$  is the complex conjugate.

3) Updating  $\mathcal{T}$  with other variables being fixed:

$$\mathcal{T}^{k+1} = \arg \min_{\mathcal{T}} \lambda_s \left\| \mathcal{T} \right\|_1 + \frac{\mu^k}{2} \left\| \mathcal{D} - \mathcal{B}^{k+1} - \mathcal{T} - \mathcal{N}^k + \frac{y_1^k}{\mu^k} \right\|_F^2. \quad (21)$$

The above problem (21) can be solved by performing element-wise shrinkage operation [51]:

$$\mathcal{T}^{k+1} = Th_{\lambda_1(\mu^k)}^{-1} \left( \mathcal{D} - \mathcal{B}^{k+1} - \mathcal{N}^k + \frac{y_1^k}{\mu^k} \right), \quad (22)$$

where  $Th(\cdot)$  is the element-wise shrinkage operator.

4) Updating  $V_1, V_2, V_3$  with other variables being fixed:

$$\begin{cases} V_1^{k+1} = \arg \min_{V_1} \lambda_{tv} \|V_1\|_1 + \frac{\mu^k}{2} \left\| V_1^k - D_h \mathcal{B}^{k+1} + \frac{y_3^k}{\mu^k} \right\|_F^2 \\ V_2^{k+1} = \arg \min_{V_2} \lambda_{tv} \|V_2\|_1 + \frac{\mu^k}{2} \left\| V_2^k - D_v \mathcal{B}^{k+1} + \frac{y_4^k}{\mu^k} \right\|_F^2 \\ V_3^{k+1} = \arg \min_{V_3} \delta \lambda_{tv} \|V_3\|_1 + \frac{\mu^k}{2} \left\| V_3^k - D_z \mathcal{B}^{k+1} + \frac{y_5^k}{\mu^k} \right\|_F^2. \end{cases} \quad (23)$$

The above problem can also be solved by element-wise shrinkage operator:

$$\begin{cases} V_1^{k+1} = Th_{\lambda_{tv}(\mu^k)}^{-1} \left( D_h \mathcal{B}^{k+1} - \frac{y_3^k}{\mu^k} \right) \\ V_2^{k+1} = Th_{\lambda_{tv}(\mu^k)}^{-1} \left( D_v \mathcal{B}^{k+1} - \frac{y_4^k}{\mu^k} \right) \\ V_3^{k+1} = Th_{\delta \lambda_{tv}(\mu^k)}^{-1} \left( D_z \mathcal{B}^{k+1} - \frac{y_5^k}{\mu^k} \right). \end{cases} \quad (24)$$

5) Updating  $\mathcal{N}^{k+1}$  with other variables being fixed:

$$\mathcal{N}^{k+1} = \arg \min_{\mathcal{N}} \lambda_3 \left\| \mathcal{N} \right\|_F^2 + \frac{\mu^k}{2} \left\| \mathcal{D} - \mathcal{B}^{k+1} - \mathcal{T}^{k+1} - \mathcal{N} + \frac{y_1^k}{\mu^k} \right\|_F^2. \quad (25)$$

The solution of the above problem can be obtained by:

$$\mathcal{N}^{k+1} = \frac{\mu^k \left( \mathcal{D} - \mathcal{B}^{k+1} - \mathcal{T}^{k+1} \right) + y_1^k}{\mu^k + 2\lambda_3}. \quad (26)$$

6) Updating multipliers  $y_1, y_2, y_3, y_4, y_5$  with other variables being fixed:

$$\begin{cases} y_1^{k+1} = y_1^k + \mu^k \left( \mathcal{D} - \mathcal{B}^{k+1} - \mathcal{T}^{k+1} - \mathcal{N}^{k+1} \right) \\ y_2^{k+1} = y_2^k + \mu^k \left( \mathcal{Z}^{k+1} - \mathcal{B}^{k+1} \right) \\ y_3^{k+1} = y_3^k + \mu^k \left( V_1^{k+1} - D_h \mathcal{B}^{k+1} \right) \\ y_4^{k+1} = y_4^k + \mu^k \left( V_2^{k+1} - D_v \mathcal{B}^{k+1} \right) \\ y_5^{k+1} = y_5^k + \mu^k \left( V_3^{k+1} - D_z \mathcal{B}^{k+1} \right). \end{cases} \quad (27)$$

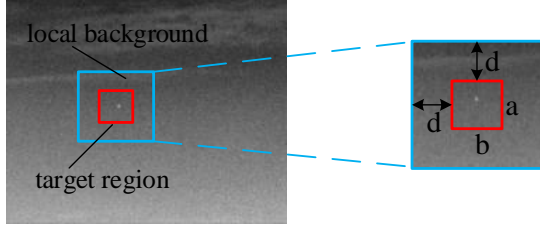


Figure 3. The neighboring background area of target.

7) Updating  $\mu^{k+1}$  by  $\mu^{k+1} = \min(\rho\mu^k, \mu_{\max})$ .

Finally, the proposed ASTTV-NTLA method is summarized in **Algorithm2**.

---

**Algorithm2:** ASTTV-NTLA Algorithm

---

**Input:** infrared image sequence  $d_1, \dots, d_P \in \mathbb{R}^{n_1 \times n_2}$ , number of frames  $L$ , parameters  $\lambda_s, \lambda_{tv}, \lambda_3, \mu > 0$

**Initialize:** Transform the image sequence into the original tensor  $\mathcal{D}, \mathcal{B}^0 = \mathcal{T}^0 = \mathcal{N}^0 = V_i^0 = 0, i = 1, 2, 3, y_i^0 = 0, i = 1, \dots, 5, \mu_0 = 1e-2, \mu_{\max} = 1e7, k = 0, \rho = 1.5, \zeta = 1e-6$ .

**While :** not converged do

1 : Update  $\mathcal{Z}^{k+1}$  by **Algorithm1**

2 : Update  $\mathcal{B}^{k+1}$  by Eq.(20)

3 : Update  $\mathcal{T}^{k+1}$  by Eq.(22)

4 : Update  $V_1^{k+1}, V_2^{k+1}, V_3^{k+1}$  by Eq.(24)

5 : Update  $\mathcal{N}^{k+1}$  by Eq.(26)

6 : Update multipliers  $y_i^{k+1}, i = 1, \dots, 5$  by Eq.(27)

7 : Update  $\mu^{k+1}$  by  
 $\mu^{k+1} = \min(\rho\mu^k, \mu_{\max})$

8 : Check the convergence conditions

$$\frac{\|\mathcal{D} - \mathcal{B}^{k+1} - \mathcal{T}^{k+1} - \mathcal{N}^{k+1}\|_F^2}{\|\mathcal{D}\|_F^2} \leq \zeta$$

9 : Update  $k = k + 1$

**end While**

**Output :**  $\mathcal{B}^{k+1}, \mathcal{T}^{k+1}, \mathcal{N}^{k+1}$

---

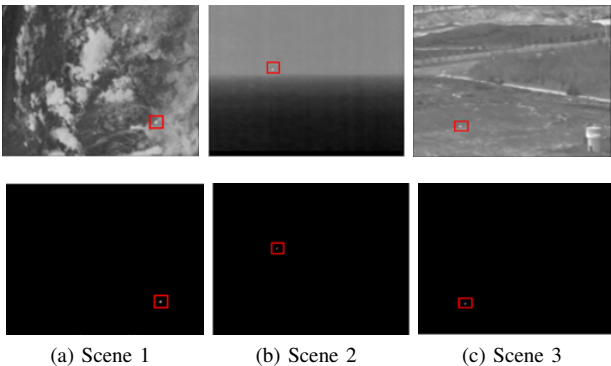


Figure 4. Single target scenes and results. Row 1: the original images. Row 2: the corresponding results without segmentation.

#### D. Target Detection procedure

In Fig. 2, we show the specific implementation procedure of the target detection method based on the proposed ASTTV-NTLA model. Meanwhile, the detailed steps are explained in the following.

1) Patch-tensor construction. The original infrared image sequence  $d_1, d_2, \dots, d_P \in \mathbb{R}^{n_1 \times n_2}$  is transformed into several patch-tensors  $\mathcal{D} \in \mathbb{R}^{n_1 \times n_2 \times n_3}$  by stacking  $n_3$  adjacent frames in chronological order.

2) Background and target separation. According to **Algorithm 2**, the original patch-tensor  $\mathcal{D}$  is decomposed into background patch-tensor  $\mathcal{B}$ , target patch-tensor  $\mathcal{T}$  and noise patch-tensor  $\mathcal{N}$ .

3) Image reconstruction. The target image  $f_T$  and background image  $f_B$  can be reconstructed by simple inverse operation.

4) Target detection. Considering that the pixels of the true targets have higher values in the reconstructed target image, small targets can be extracted via a simple adaptive threshold segmentation algorithm [22].

$$t_{th} = \max(v_{\min}, \mu + k\sigma) \quad (28)$$

where  $\mu$  and  $\sigma$  are the mean and standard deviation of the target image  $f_T$ , respectively.  $k$  is a constant determined experimentally.  $v_{\min} = 0.85$  is an adaptive value. A pixel at  $(x, y)$  can be segmented as target if  $f_T(x, y) > t_{th}$ .

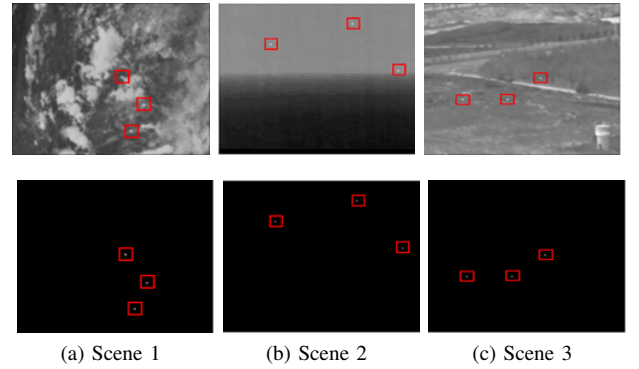


Figure 5. Multiple target scenes and results. Row 1: the original images. Row 2: the corresponding results without segmentation.

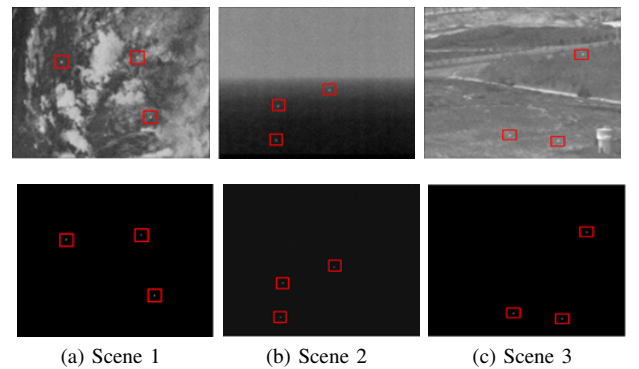
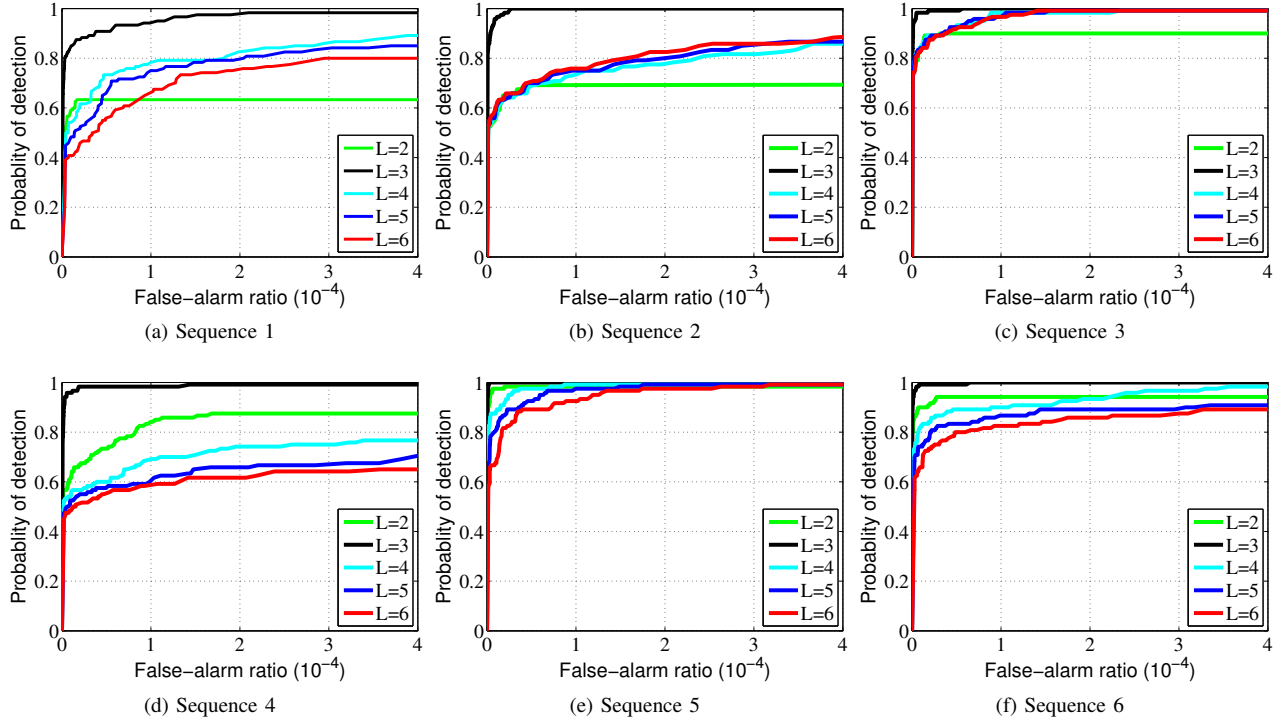


Figure 6. Noisy multiple target scenes and results. Row 1: the original images. Row 2: the corresponding results without segmentation.

#### E. Complexity analyses

The computational complexity of the proposed method is briefly discussed here. For the input image sequence  $d_1, d_2, \dots, d_P \in \mathbb{R}^{n_1 \times n_2}$ , we can obtain  $s = p/n_3$ , and the dimension of each tensor is  $\mathcal{D} \in \mathbb{R}^{n_1 \times n_2 \times n_3}$ . In ASTTV-NTLA algorithm, the main cost is to update  $\mathcal{Z}$  and  $\mathcal{B}$ , and the optimization of other variables can be solved by simple

Figure 7. ROC curves with respect to different  $L$ .Table I  
DETAILED PARAMETER SETTING FOR TESTED METHODS.

Methods	Acronyms	Parameter settings
Top-Hat method	Top-Hat	Structure shape: square, structure size: $3 \times 3$
Weighted strengthened local contrast measure	WSLCM	$K = 9$ , gaussian filter size: $3 \times 3$
multiscale tri-layer local contrast measure	TLLCM	$K = 9$ , gaussian filter size: $3 \times 3$
Infrared Patch-Image Mode	IPI	Patch Size: $50 \times 50$ , sliding step: 10, $\lambda = \frac{1}{\sqrt{\max(M, N)}}$ , $\gamma = 0.002$ , Patch Size: $50 \times 50$ , sliding step: 10, $\lambda = \frac{1}{\sqrt{\max(M, N)}}$ , $\gamma = 0.002$ , $\mu^0 = 3\sqrt{\min(M, N)}$ , $C = \sqrt{\min(M, N)}/2.5$ , $\varepsilon = 1e-7$
Non-Convex Rank Approximation Minimization	NRAM	Patch Size: $30 \times 30$ , sliding step: 30, $\lambda = \frac{3}{\sqrt{\max(M, N)}}$ , $\varepsilon = 1e-7$
Stable multisubspace learning	SMSL	$\lambda_1 = 0.005$ , $\lambda_2 = \frac{1}{\sqrt{\max(M, N)}}$ , $\beta = 0.025$ , $\gamma = 1.5$
Total Variation Regularization and Principal Component Pursuit	TV-PCP	Patch Size: $50 \times 50$ , sliding step: 10, $\lambda = \frac{L}{\sqrt{\min(n_1, n_2, n_3)}}$ , $L = 1$ , $h = 10$ , $\varepsilon = 1e-7$
Reweighted Infrared Patch-Tensor Model	RIPT	Patch Size: $40 \times 40$ , sliding step: 40, $\lambda = \frac{0.6}{\sqrt{\max(n_1, n_2) * n_3}}$ , $\varepsilon = 1e-7$
Partial Sum of the Tensor Nuclear Norm	PSTNN	$L = 3$ , $H = 8$ , $\lambda_1 = 0.005$ , $\lambda_2 = \frac{H}{\sqrt{\max(M, N) * L}}$ , $\lambda_3 = 100$
Spatial-temporal Total Variation Regularization and weighted Tensor Nuclear Norm	STTV-WNIPT	$L = 3$ , $H = 6$ , $\lambda_{tv} = 0.005$ , $\lambda_s = \frac{H}{\sqrt{\max(M, N) * L}}$ , $\lambda_3 = 100$
Non-Convex Tensor Low-Rank Approximation for Infrared Small Target Detection	ASTTV-NTLA	

linear calculation. Updating  $\mathcal{Z}$  requires performing FFT and  $\lceil \frac{n_3+1}{2} \rceil$  SVDs of  $n_1 \times n_2$  matrices in each iteration by t-SVT, which cost  $\mathcal{O}(ksn_1n_2n_3(\log n_3 + (n_2 \lceil \frac{n_3+1}{2} \rceil)/n_3))$ . Updating  $\mathcal{B}$  requires performing FFT operation, which cost  $\mathcal{O}(ksn_1n_2n_3 \log(n_3))$ . The  $k$  denotes the iteration times. In summary, the computational cost at each iteration is  $\mathcal{O}(ksn_1n_2n_3(2\log n_3 + (n_2 \lceil \frac{n_3+1}{2} \rceil)/n_3))$ .

## V. EXPERIMENTAL RESULTS AND ANALYSES

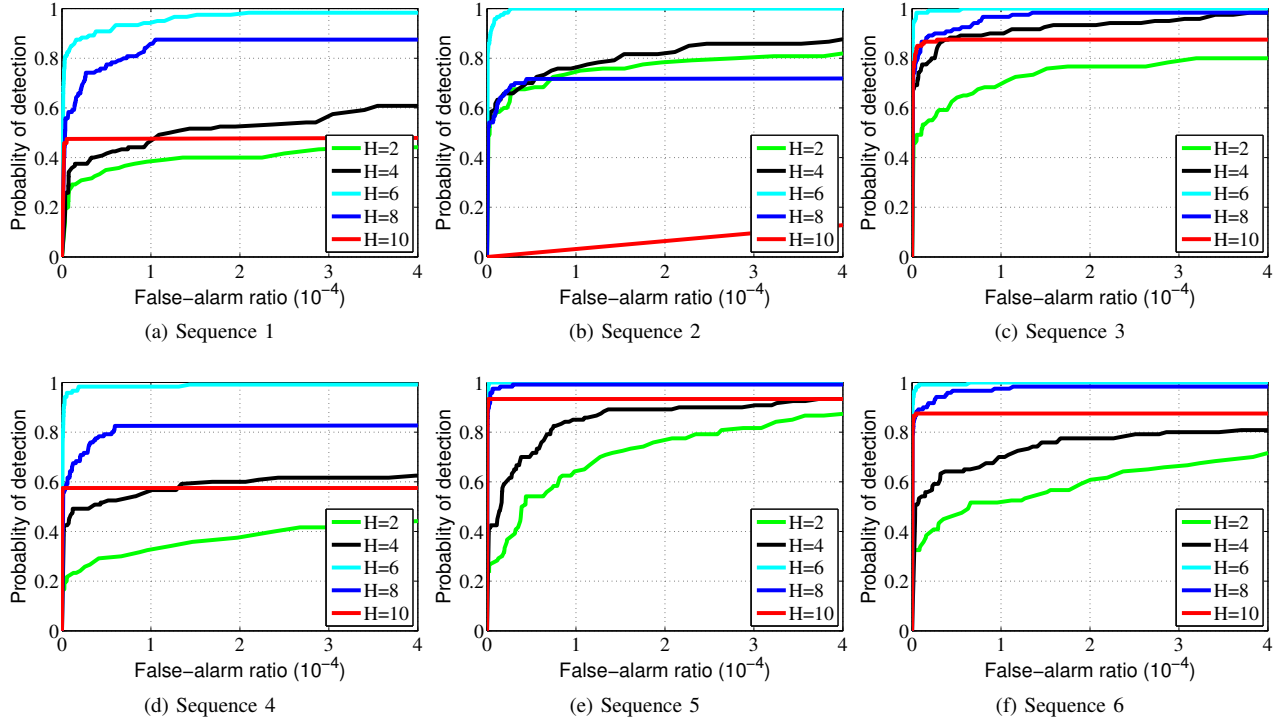
In this section, we first introduce the evaluation metrics and baseline methods, then discuss the key parameters of our method. Finally, we compare the performance of our method with the baseline methods.

### A. Evaluation Metrics and Baseline Methods

For a comprehensive evaluation, four metrics including the local signal to noise ratio gain (LSNRG), background suppression factor (BSF), signal to clutter ratio gain (SCRG) and contrast gain (CG) are used to evaluate the background suppression ability and detection performance. LSNRG measures the local signal to noise ratio (LSNR) gain, which is defined as

$$\text{LSNRG} = \frac{\text{LSNR}_{\text{out}}}{\text{LSNR}_{\text{in}}}, \quad (29)$$

where  $\text{LSNR}_{\text{out}}$  and  $\text{LSNR}_{\text{in}}$  are the LSNR values before and after processing, and  $\text{LSNR} = P_T/P_B$ .  $P_T$  and  $P_B$  are the maximum pixel values of the target and neighborhood, respectively. Then the background suppression factor (BSF) is

Figure 8. ROC curves with respect to different  $H$ .

used to compare the background suppression ability, which is defined as:

$$\text{BSF} = \frac{\sigma_{\text{in}}}{\sigma_{\text{out}}}, \quad (30)$$

where  $\sigma_{\text{in}}$  and  $\sigma_{\text{out}}$  are the standard variance of the neighboring background region of original image and target image, respectively. The most widely used SCRG is defined as the ratio of signal-to-clutter ratio (SCR) before and after processing:

$$\text{SCRG} = \frac{\text{SCR}_{\text{out}}}{\text{SCR}_{\text{in}}}, \quad (31)$$

where SCR is defined as follows [52]:

$$\text{SCR} = \frac{|\mu_t - \mu_b|}{\sigma_b}, \quad (32)$$

where  $\mu_t$  is the average value of the target area,  $\mu_b$  and  $\sigma_b$  are the average pixel value and standard deviation of the surrounding local neighborhood region, respectively. The size of neighboring background region is  $(a + 2d) \times (b + 2d)$ , where  $a \times b$  and  $d$  represent the size of target region and the width of neighboring area, as illustrated in Fig. 3. We use contrast gain (CG) [53] to compare the ability to expand gray level difference between the target and background, which is defined as below:

$$\text{CG} = \frac{\text{CON}_{\text{out}}}{\text{CON}_{\text{in}}}, \quad (33)$$

where  $\text{CON}_{\text{in}}$  and  $\text{CON}_{\text{out}}$  are the contrast (CON) of the original and target images, respectively, and CON is defined as:

$$\text{CON} = |\mu_t - \mu_b|, \quad (34)$$

where  $\mu_t$  and  $\mu_b$  are the same as those in Eq. (32). In general, higher values means better background suppression

ability for the above four metrics, and it should be noted that LSNRG, BSF and SCRG only evaluate the suppression ability in local neighboring area, but not globally. Among all the existing metrics, the detection probability  $P_d$  and false-alarm rate  $F_a$  are the key performance indicators, which are defined as follows [22]:

$$P_d = \frac{\text{number of true detections}}{\text{number of actual targets}} \quad (35)$$

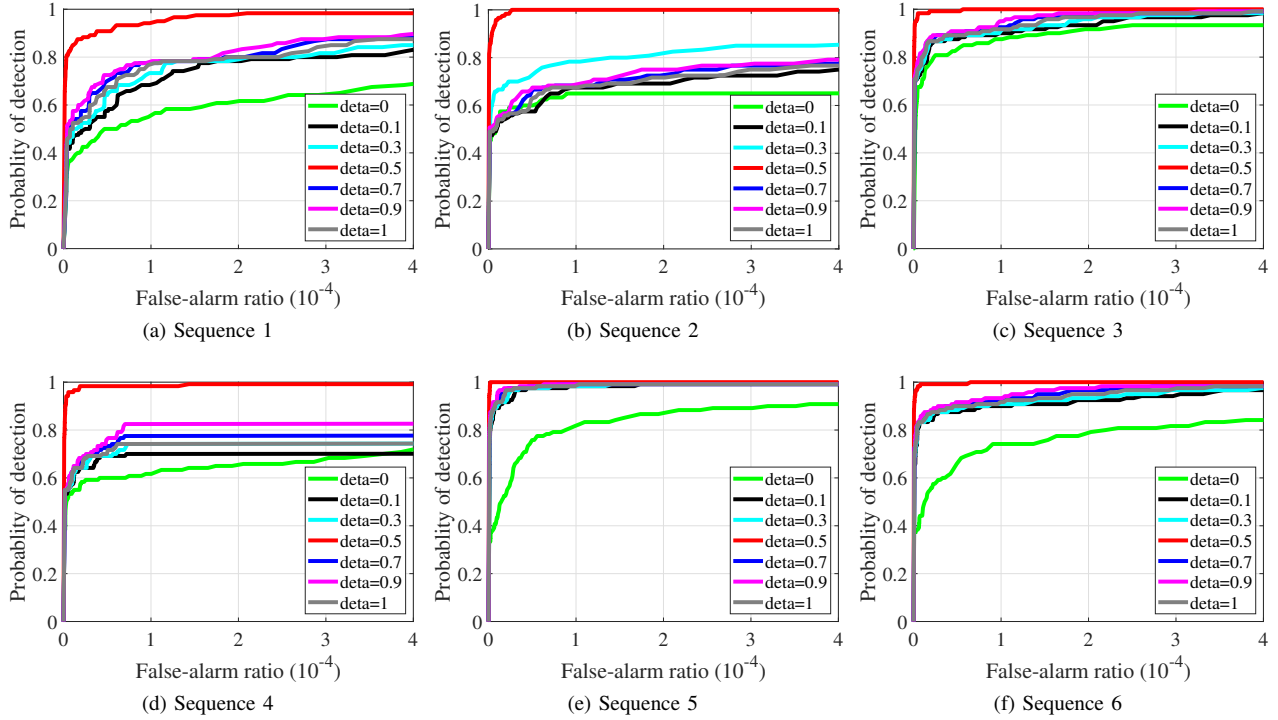
$$F_a = \frac{\text{number of false detections}}{\text{number of image pixels}}. \quad (36)$$

The above two indicators range between 0 and 1.

To further evaluate the effectiveness of the proposed method, we compare its performance with ten state-of-the-art methods, which are BS-based methods (Top-Hat [12]), HVS-based methods (WSLCM [18], TLLCM [19]), and recently developed LRSD-based methods (IPI [22], NRAM [26], SMSL [29], TV-PCP [31], RIPT [4], PSTNN [5], STTV-WNIPT [8]). Table I summarizes all the methods involved in the experiments and their detailed parameter settings. All the algorithms are implemented in MATLAB 2014a on a PC of 4.4 GHz and 16GB RAM.

### B. Parameter Setting and Datasets

The parameters in our model have a key influence on target detection performance. By testing the synthetic data, we have chosen the appropriate values for each parameter. The regularized parameter  $\lambda_{tv}$  could balance the tradeoff between the non-convex tensor low-rank approximation and ASTTV regularization, and it is empirically set to 0.005 following [47].  $\delta$  is set in the range of [0,1] for most of the cases, we follow [48] to set  $\delta = 0.5$ . The parameter  $\lambda_s$  is used to control the

Figure 9. ROC curves with respect to different  $\delta$ .Table II  
CHARACTERISTICS OF THE DATASET.

Sequence	Frames	Image Size	Target Size	Average SCR	Target Descriptions	Background Descriptions
1	120	$200 \times 250$	$3 \times 4 \sim 3 \times 6$	4.79	Fast-moving, tiny, regular shape	scenario with multilayer cloud, heavy noise
2	120	$200 \times 300$	$4 \times 4 \sim 5 \times 5$	3.89	Fast-moving, irregularly shaped aircraft	Fierce clouds and heavy noise
3	120	$200 \times 250$	$4 \times 3 \sim 4 \times 6$	3.51	Small and dim, quick motion	A blurred sealand background with a strong reflective artificial building
4	120	$250 \times 250$	$3 \times 3 \sim 5 \times 5$	2.33	Dim and slow-moving airplane	Mountains with strong reflections
5	120	$250 \times 250$	$3 \times 3 \sim 3 \times 6$	1.83	Small and slow-moving airplane	village, reflective road and roof
6	120	$250 \times 250$	$4 \times 3 \sim 5 \times 4$	2.64	Small and slow-moving airplane	Forest, reflective road and roof

relative contribution of sparse term. And we follow [54] to set  $\lambda_s = \frac{H}{\sqrt{\max(m,n) \times L}}$ , where  $H$  denotes a tuning parameter. The parameter  $\lambda_3$  is set to 100 following [55]. In the following experiments, we set the number of frames  $L = 3$ . Moreover, we also conduct experiments to further analyze the influence of parameter  $L$ ,  $H$  and  $\delta$ . Please refer to Section IV-D for more details.

To evaluate the detection ability and stability of the proposed method under diverse backgrounds, We simulate six image sequences that come from various scenes, as given in Table II. The synthetic data are created using six real background data and simulated target data. Note that, we generate the synthetic targets by using the approach in method [22]. In Sequence 1, the target is a fast-moving, regular shaped aircraft with a heavy sky cluttered background. In Sequence 2, a small and irregularly shaped aircraft is moving with fierce clouds and heavy noise. In Sequence 3, a small target is moving with a blurred sealand background, and there exists a brighter artificial building. In Sequence 4, the target is an airplane flying towards the mountains, and the bottom of the infrared image is mountains with strong reflections. In Sequence 5, the target is a small, slow aircraft flying through the village with reflective roofs and roads in the background.

In Sequence 6, the target is a small slow aircraft flying in the forest with a reflection road in the background. The 2D and 3D gray distributions of representative images are also shown Figs. 10 and 11 and Figs. 12 and 13.

### C. Validation of the proposed ASTTV-NTLA method

In this subsection, we validate the robustness of the proposed method in various scenes.

1) Robustness to single targets scene: Firstly, the proposed method is tested on three real single target infrared image sequences. The representative images are given in the first row of Fig. 4, and the corresponding separated target images are shown in the second row. For better visualization, the targets are labeled with red boxes. It can be observed from Fig. 4 that the background clutters are suppressed perfectly and each target is detected successfully.

2) Robustness to multiple targets scene: In a variety of real scenes, the number of targets of interest is different, such as a fleet and multiple independently guided reentry vehicles (MIRVs). Therefore, we test the performance of ASTTV-NTLA method in multi-objective scenario (actually 3). It is worth noting that we adopt a method similar to [22] to synthesize multi-target scenes. The synthetic images are given



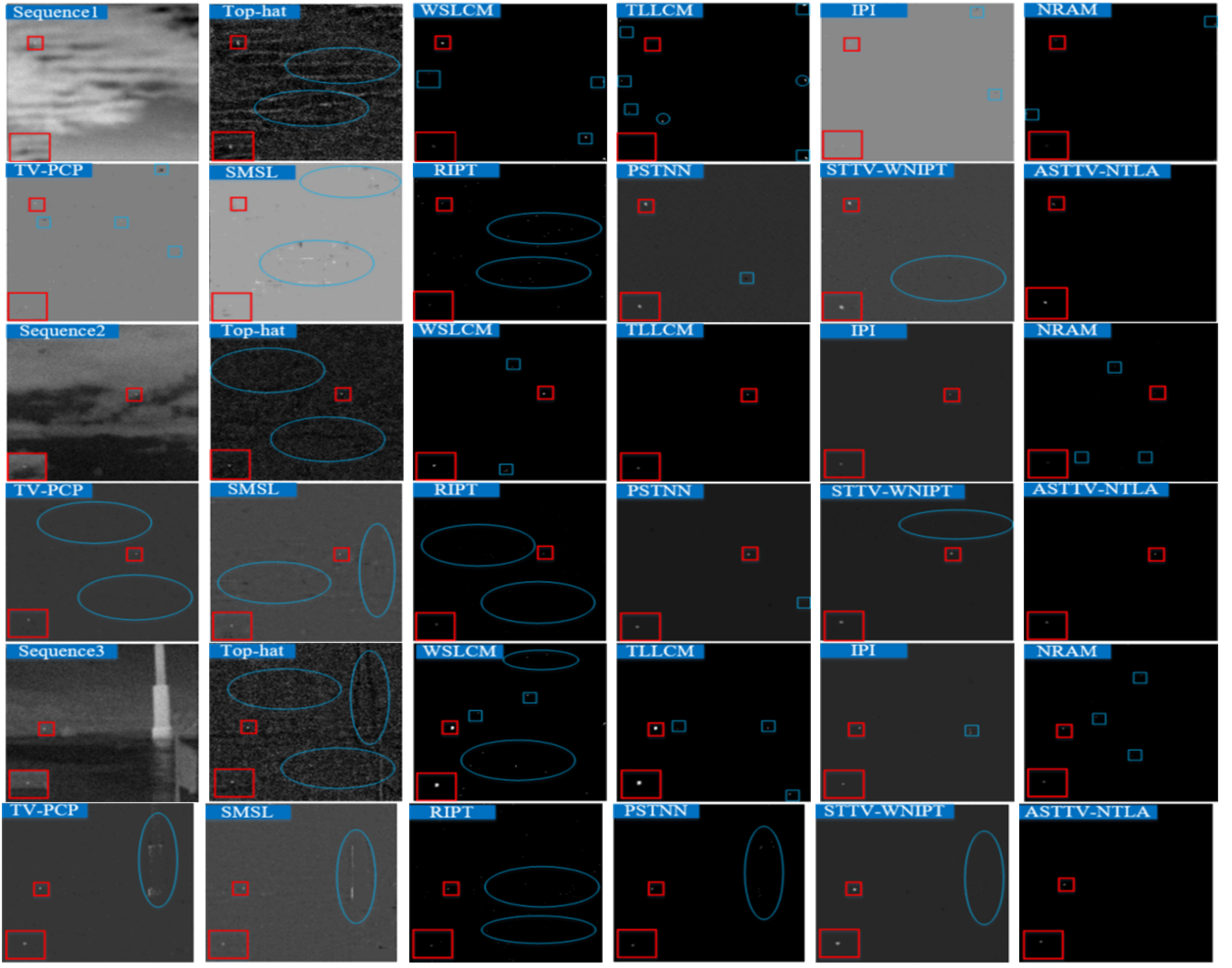


Figure 10. Comparative results achieved by different methods on Sequence 1-3 (without segmentation). The blue ellipses represent background residuals and noise. For better visualization, the demarcated target area is zoomed in the left bottom corner.

in the first row of Fig. 5, and it can be seen from the second row of Fig. 5 that the background clutters are suppressed clearly.

3) Robustness to noisy scene: In real scenes, noise is another important factor that affects the performance of target detection. Therefore, ASTTV-NTLA method is tested on several noisy scenarios. Firstly, we add Gaussian noise with  $\sigma = 15$  to the original images, as shown in the first row of Fig. 6. The results in the second row of Fig. 6 show that ASTTV-NTLA method can suppress clutter and noise better when  $\sigma = 15$ .

#### D. Parameter Analysis

In this subsection, we analyze the influence of number of frame  $L$ , tuning parameter  $H$ , and parameter  $\delta$  on the performance of the method.

1) Number of frames: We exploit ASTTV regularization to utilize the temporal information, and the number of frames  $L$  is a key parameter. We vary  $L$  from 2 to 6 with a step of 1. The corresponding ROC curves are shown in Fig. 7. It can be observed that the performance is the best when  $L = 3$ . It is worth noting that if the value of the  $L$  is too small,

the detection probability will decrease. At the same time, the low-rank assumption could fail when  $L$  is too large, and the performance of the proposed method would degrade. To achieve a balance between the performance and effectiveness, we set  $L = 3$  in the following experiments, and we find it works well for all the experiments.

2) Tuning parameter: Weighting parameter plays an important role in the optimization process of the model. We vary tuning parameter  $H$  from 2 to 10 with a step of 2, and the corresponding ROC curves are also given in Fig. 8. It can be observed from Figs. 8 (a) and (b) that the ROC curves of  $H = 10$  demonstrate that an over-large  $H$  will decrease the detection probability. Meanwhile, from the results of  $H = 2$  and  $H = 4$  in Figs. 8 (a), (d) and (f), we can conclude that an over-small  $H$  will increase the false alarm rate. So we set  $H = 6$  in the following experiments, and it should be noted that it is possible to further improve the performance by tuning  $H$  more carefully.

3) Parameter  $\delta$ :  $\delta$  has an impact on the detection results. It means that the temporal difference in the ASTTV regularization contributes to improving the performance of the proposed method. We vary  $\delta$  from 0 to 1 with a step of 0.2, and the

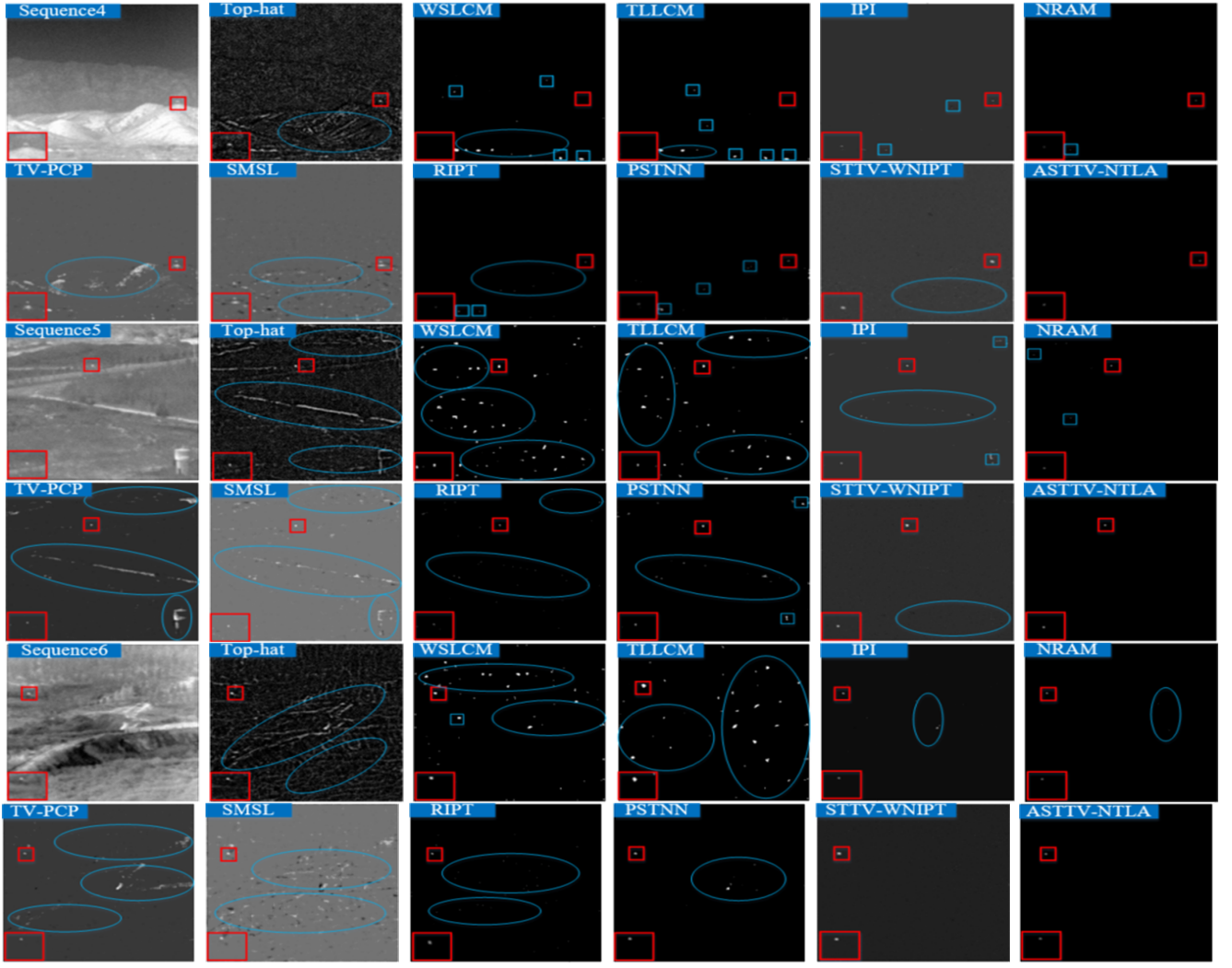


Figure 11. Comparative results achieved by different methods on Sequence 4-6 (without segmentation). The blue ellipses represent background residuals and noise. For better visualization, the demarcated target area is zoomed in the left bottom corner.

corresponding ROC curves are also given in Fig. 9. As shown in Fig. 9, the ROC curves of  $\delta = 0$  demonstrate that the detection probability will be reduced if there is no temporal information.  $\delta = 1$  is STTV regularization. As can be seen from Fig. 9, selecting the appropriate  $\delta$  value will get better detection performance. So we set  $\delta = 0.5$  in the following experiments, and it should be noted that it is possible to further improve the performance by tuning  $\delta$  more carefully.

#### E. Comparison to state-of-the-art Methods

To compare the performance of the proposed method and other ten state-of-the-art methods, we conduct extensive experiments on six real infrared image sequences. Figs. 10 and 11 show the comparative results of Sequences 1-6. In these figures, we can see that the detection results of Top-hat is very rough. Top-hat method not only enhances the target on Sequences 1-6, but also enhances the clutters and noises. For example, the residuals of reflective mountains of Sequence 4 and road of Sequence 5 are still remained in the results. The main reason is that the filter size of Top-hat is not suitable for the scenes with strong reflection clutter. As a top-performing HVS method, WSLCM and TLLCM can detect

the target more accurately in simple background, but there are still clutter or missed detection in complex background. IPI is a classical LRSD method. Compared with the BS and HVS method, IPI has less background residual or missed clutter in complex background. Therefore, it promotes the development of NRAM, TV-PCP and SMSL methods. From the highlight scene Sequence 4 and the complex ground scene Sequences 5-6, it can be seen that IPI and NRAM method still have a little residual and clutter, but TV-PCP and SMSL methods achieve poor performance on these complex scenes. To solve the above problems, RIPT directly stacks the patches into a patch-tensor, which successfully converts a low-rank matrix recovery into a tensor recovery problem. It can be seen from the experimental results that RIPT method can suppress the clutters more clearly than matrix-based methods. Therefore, many improved methods are proposed, such as PSTNN and STTV-WNIPT. As can be seen from Fig. 10, these tensor-based methods can suppress clutter in complex background, but some non-target pixels still remain in their target image. In contrast, the proposed method can detect targets accurately under the premise of better suppression of background and



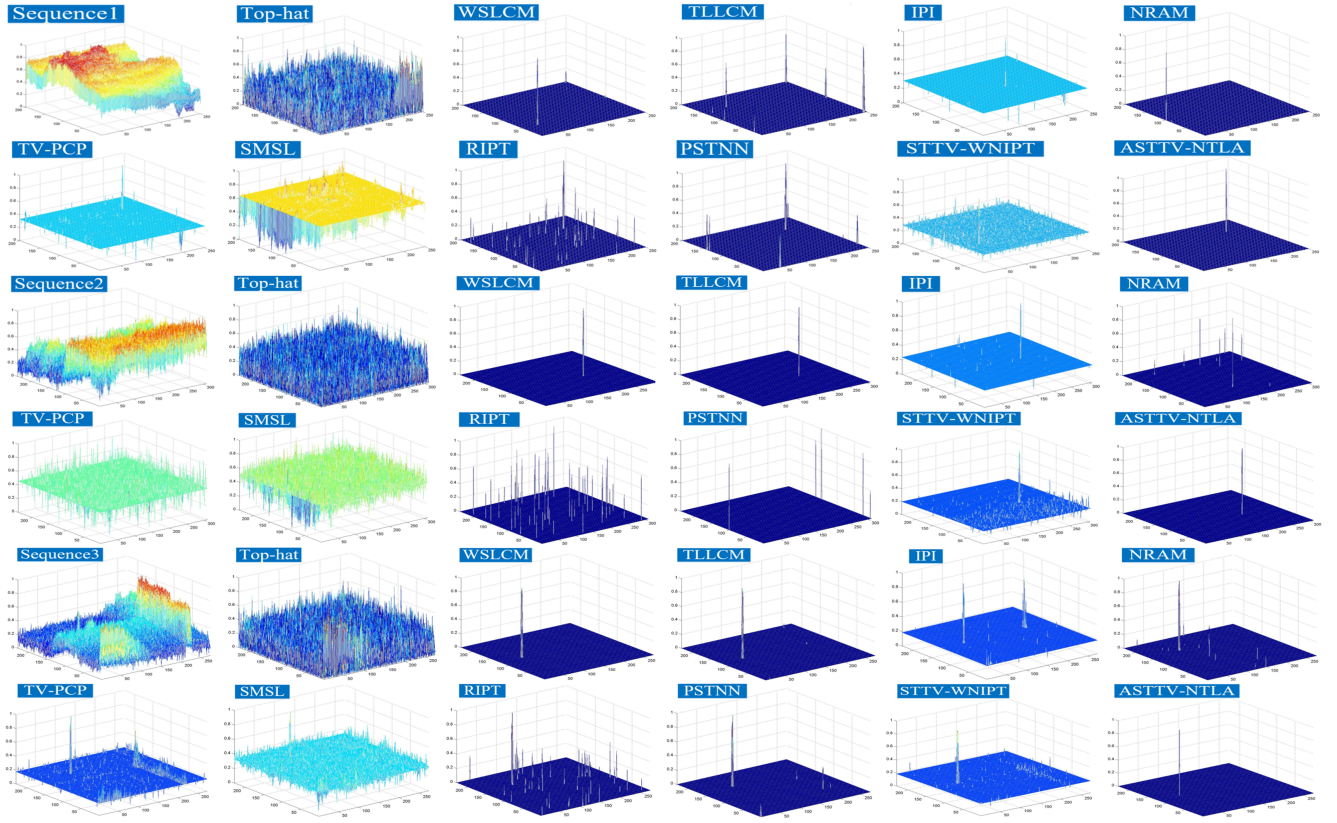


Figure 12. 3D display of results achieved by different methods in Sequence 1-3.

Table III  
QUANTITATIVE COMPARISON OF DIFFERENT METHODS ON SEQUENCES 1-3.

Method	60th frame of Sequence 1			100th frame of Sequence 2			90th frame of Sequence 3		
	LSNRG	BSF	SCRG	LSNRG	BSF	SCRG	LSNRG	BSF	SCRG
<b>Top-hat</b> [12]	0.59	0.77	0.33	0.85	1.27	0.13	0.37	0.71	0.26
<b>WSLCM</b> [18]	1.15	2.18	41.69	1.02	3.06	4.26	1.44	2.46	4.36
<b>TLLCM</b> [19]	NaN	<b>Inf</b>	NaN	1	5.64	7.93	0.98	1.13	4.51
<b>IPI</b> [22]	1.91	27.01	111.42	1.08	7.36	10.74	1.11	4.56	3.51
<b>NRAM</b> [26]	<b>Inf</b>	<b>Inf</b>	<b>Inf</b>	NaN	<b>Inf</b>	NaN	1.28	4.74	4.36
<b>TV-PCP</b> [31]	1.64	5.10	24.13	1.02	4.85	6.53	1.11	4.13	3.39
<b>SMSL</b> [29]	1.29	4.91	18.96	0.93	5.73	2.94	1.02	3.24	1.81
<b>RIPT</b> [4]	<b>Inf</b>	<b>Inf</b>	<b>Inf</b>	1.05	5.73	8.05	1.12	3.60	3.00
<b>PSTNN</b> [5]	<b>Inf</b>	<b>Inf</b>	<b>Inf</b>	0.94	4.65	12.73	1.19	3.73	4.36
<b>STTV-WNIPT</b> [8]	1.48	1.88	42.50	2.03	3.85	11.14	1.82	3.86	22.90
<b>ASTTV-NTLA (ours)</b>	<b>Inf</b>	<b>Inf</b>	<b>Inf</b>	<b>11.02</b>	<b>14.42</b>	<b>25.24</b>	<b>Inf</b>	<b>Inf</b>	<b>Inf</b>

noise. The results validate the effectiveness of the ASTTV and non-convex tensor low-rank approximately property. Note that the dataset contains a variety of scenes, so the experimental results can demonstrate the robustness and superiority of the proposed method. Moreover, we show the 3D maps in Figs. 12 and 13 for an intuitive comparison. It can be seen from Figs. 12 and 13 that the proposed method can better enhance the target and suppress the clutter.

In this paper, we use LSNRG, SCRG and BSF to perform quantitative analyses of different methods on the representative images of Figs. 10 and 11, and the results are listed in Table III and Table IV. We can observe that the indicator values of the proposed method are higher than other compared methods, which demonstrates that the proposed method can

better highlight the targets while suppressing the clutters and noise. Note that the **Inf** in LSNRG, BSF and SCRG denotes that the gray values of the neighboring background region are very close to zero after processing, and it only represents the local region. We can also see this situation in the results of NRAM, RIPT, PSTNN and ASTTV-NTLA method on Sequence 1. The NaN of NRAM method on Sequence 2 and TLLCM method on Sequence 1 and Sequence 4 denotes that they missed the targets. To solve this problem, we adopt the CG metric [53] that measures the ability to expand gray value difference between the background and the targets. The average CG value over the whole sequence is listed in Table V. From the result, we can observe that the proposed method achieves the highest average CG value on Sequences 1-6. The

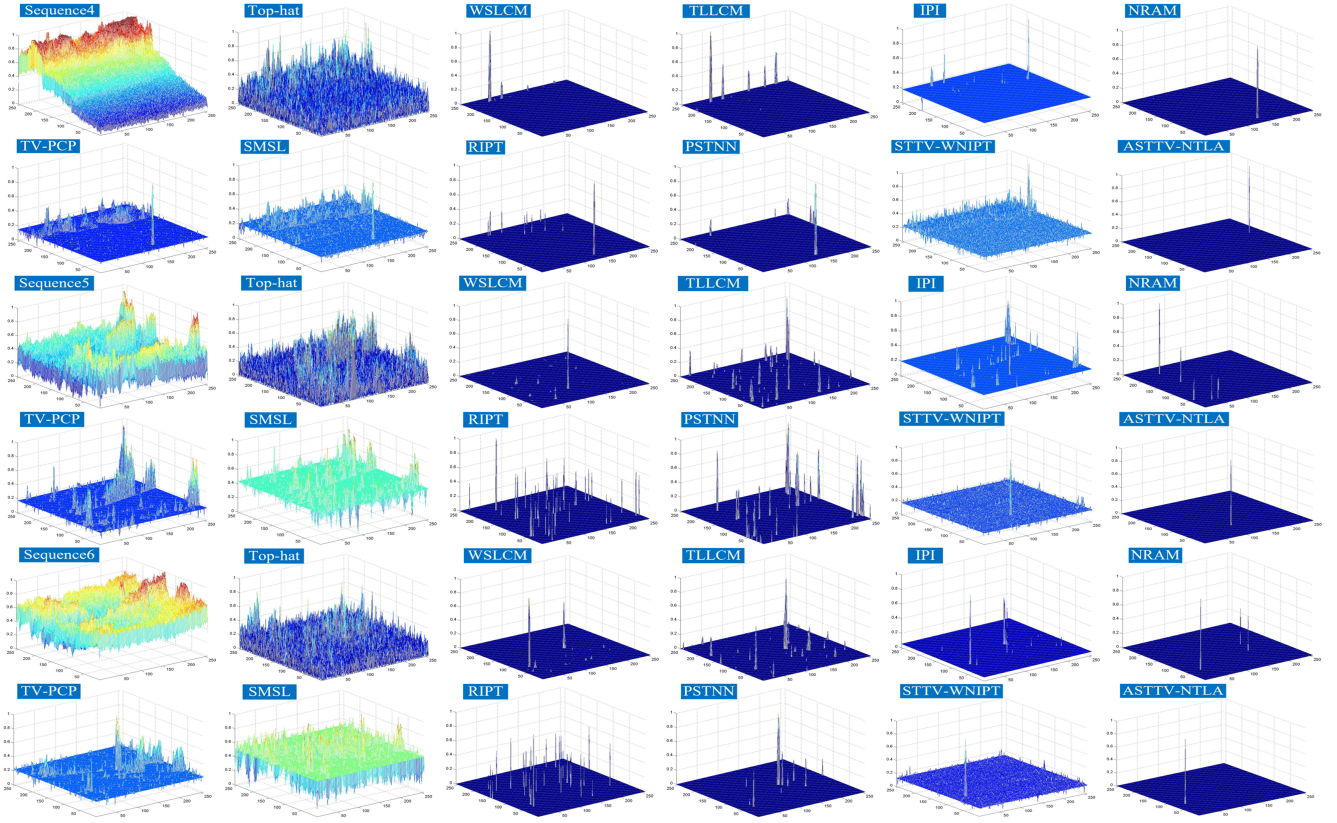


Figure 13. 3D display of results achieved by different methods in Sequence 4-6.

Table IV  
QUANTITATIVE COMPARISON OF DIFFERENT METHODS ON SEQUENCES 4-6.

Method	50th frame of Sequence 4			10th frame of Sequence 5			90th frame of Sequence 6		
	LSNRG	BSF	SCRG	LSNRG	BSF	SCRG	LSNRG	BSF	SCRG
<b>Top-hat</b> [12]	0.66	1.27	4.49	0.42	0.81	0.04	0.44	1.56	0.23
<b>WSLCM</b> [18]	NaN	<b>Inf</b>	NaN	0.73	1.52	5.13	1.14	0.98	5.20
<b>TLLCM</b> [19]	NaN	<b>Inf</b>	NaN	0.95	2.15	6.45	0.83	0.92	2.51
<b>IPI</b> [22]	3.16	24.93	164.88	2.31	24.17	22.59	1.88	6.12	13.78
<b>NRAM</b> [26]	<b>Inf</b>	<b>Inf</b>	<b>Inf</b>	<b>Inf</b>	<b>Inf</b>	<b>Inf</b>	2.66	10.33	19.79
<b>TV-PCP</b> [31]	1.44	3.05	30.55	1.47	8.17	7.77	1.51	3.82	6.34
<b>SMSL</b> [29]	1.12	2.51	27.78	1.05	5.24	4.90	1.29	2.54	4.91
<b>RIPT</b> [4]	<b>Inf</b>	<b>Inf</b>	<b>Inf</b>	2.23	9.23	9.03	2.34	5.92	18.44
<b>PSTNN</b> [5]	2.15	7.99	76.79	1.29	3.49	6.11	1.75	3.43	10.25
<b>STTV-WNIPT</b> [8]	3.45	18.93	107.49	2.09	3.68	4.54	1.36	2.86	9.92
<b>ASTTV-NTLA (ours)</b>	<b>Inf</b>	<b>Inf</b>	<b>Inf</b>	<b>Inf</b>	<b>Inf</b>	<b>Inf</b>	<b>4.76</b>	<b>19.14</b>	<b>24.89</b>

results of these indicator validate the background suppression ability of the proposed method.

Then the ROC curves of different methods are shown in Fig. 14. We can observe from the results that the proposed method achieves better performance than other methods. Top-hat method is sensitive to noise and bright clutters. WSLCM and TLLCM method achieve better detection performance on simple background scenes such as Sequence 1-3, and worse detection performance on highlighted and complex ground background scenes such as Sequence 4-6. The performance of IPI methods are slightly better than that of Top-hat, WSLCM and TLLCM methods, and the ROC curve of IPI method on Sequence 4 and Sequence 6 validate that its performance will degrade significantly in non-smooth scenarios. The perfor-

mance of the SMSL method is not good except on Sequence 3 and Sequence 5, this is because it only uses spatial information and strict orthogonal constraint dictionary. It can be seen from Sequence 4 and 6 that the detection performance of PSTNN method is poor, because it only truncates some large singular values and has the same weight for the retained small singular values, which leads to poor performance in complex scenes. The STTV-WNIPT method uses both spatial and temporal information of image sequence, and its performance is better than spatial information based methods (IPI, NRAM, TV-PCP, SMSL, RIPT, PSTNN), but there are still some residuals. The Pd of the proposed method reaches 1 fastest among all tested methods, especially on Sequences 3-6, since it considers the temporal correlation and integrating Laplace

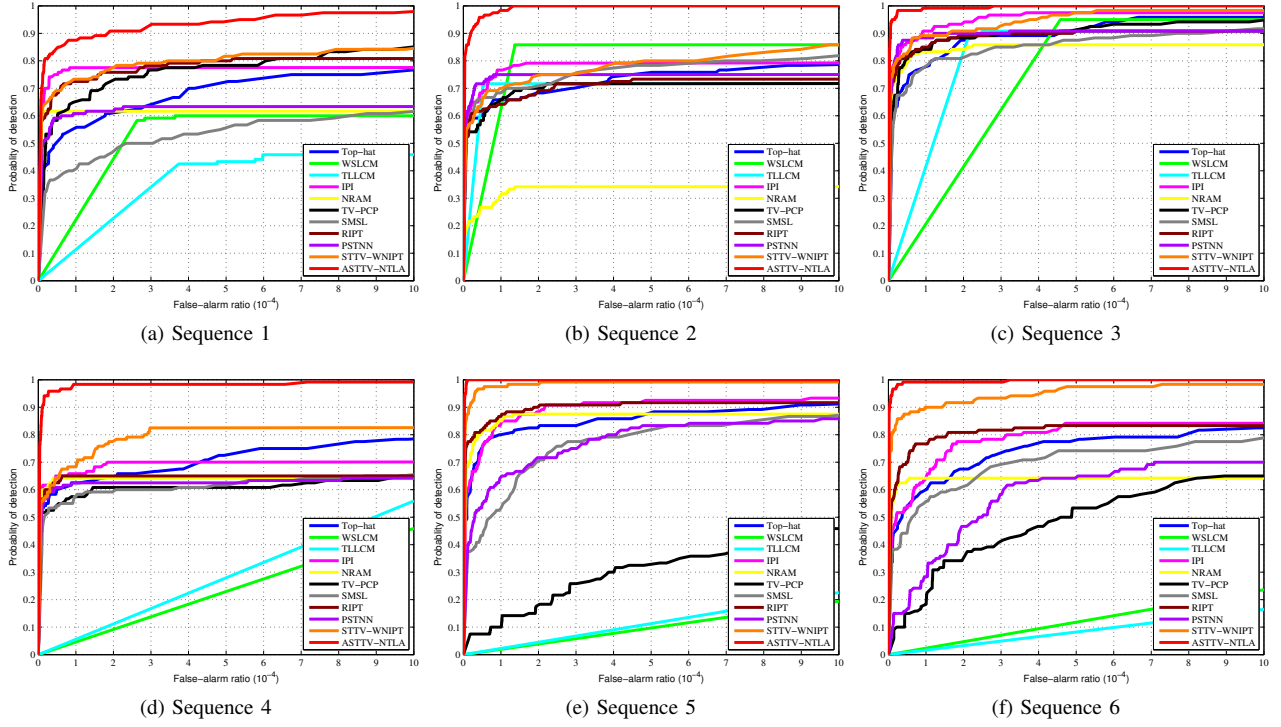


Figure 14. ROC curves achieved by different methods.

Table V  
AVERAGE CG VALUES ACHIEVED BY DIFFERENT METHODS ON SEQUENCES 1-6

Methods	Sequence 1	Sequence 2	Sequence 3	Sequence 4	Sequence 5	Sequence 6
<b>Top-hat</b> [12]	1.78	1.12	1.35	3.52	1.05	1.79
<b>WSLCM</b> [18]	9.05	1.39	3.98	2.68	3.37	1.87
<b>TLLCM</b> [19]	9.03	1.41	3.96	2.76	3.01	1.16
<b>IPI</b> [22]	4.13	1.46	1.77	6.61	1.93	2.59
<b>NRAM</b> [26]	9.63	1.02	1.92	7.90	1.74	1.07
<b>TV-PCP</b> [31]	4.73	1.35	1.82	10.03	1.95	1.32
<b>SMSL</b> [29]	3.86	1.75	1.56	11.18	1.94	2.29
<b>RIPT</b> [4]	9.63	1.41	1.83	7.89	1.98	2.68
<b>PSTNN</b> [5]	25.97	2.74	1.17	9.61	1.75	2.07
<b>STTV-WNIPT</b> [8]	22.62	2.89	1.91	9.68	1.69	7.04
<b>ASTTV-NTLA (ours)</b>	<b>28.50</b>	<b>3.45</b>	<b>5.21</b>	<b>27.33</b>	<b>3.63</b>	<b>8.46</b>

norm with ASTTV regularization, which has satisfying and robust performance under various scenes, especially for highly heterogeneous scenes and complex ground scenes.

#### F. Ablation Experiments

In this subsection, we conducted ablation experiments to verify the effectiveness of ASTTV-NTLA. The proposed model includes three terms: the spatial-temporal tensor structure, the asymmetric spatial-temporal TV regularization and nonconvex low-rank tensor approximation method. Therefore, we compare the performance of three versions of the proposed model with the proposed model, including: 1) the spatial and temporal tensor structure with the spatial-temporal TV regularization (STTV-WNIPT); 2) the asymmetric spatial-temporal TV regularization with the weighted IPT model (ASTTV-WNIPT); 3) the asymmetric spatial-temporal TV regularization with the non-convex low-rank tensor approximation (ASTTV-NTLA). The corresponding ROC curves of the above versions on Sequences 1-6 are given in Fig. 15. Moreover, the performance of ASTTV-WNIPT is better than that of

STTV-WNIPT, which demonstrates that ASTTV regularization can improve the detection ability of the model to a certain extent by using different smoothness strength for spatial TV and temporal TV. As can be seen from Fig. 15, the performance of ASTTV-NTLA is better than that of ASTTV-WNIPT. Compared with WNIPT regularization, Laplace norm exploits the sum of Laplace functions of singular values as a better substitute for tensor rank, which can obtain more accurate background estimation and further improve the ability of target detection. In summary, the above experimental results demonstrate that integrating Laplace norm with ASTTV regularization can achieve better target detection performance.

#### G. Running time

In addition to good detection ability, computational time is an important factor to be considered. However, it is hard to balance good detection ability and real-time performance. In this section, we compare the efficiency of different methods on six real infrared image sequences, and the results are given in Table VI. Top-hat is the fastest among all tested methods,



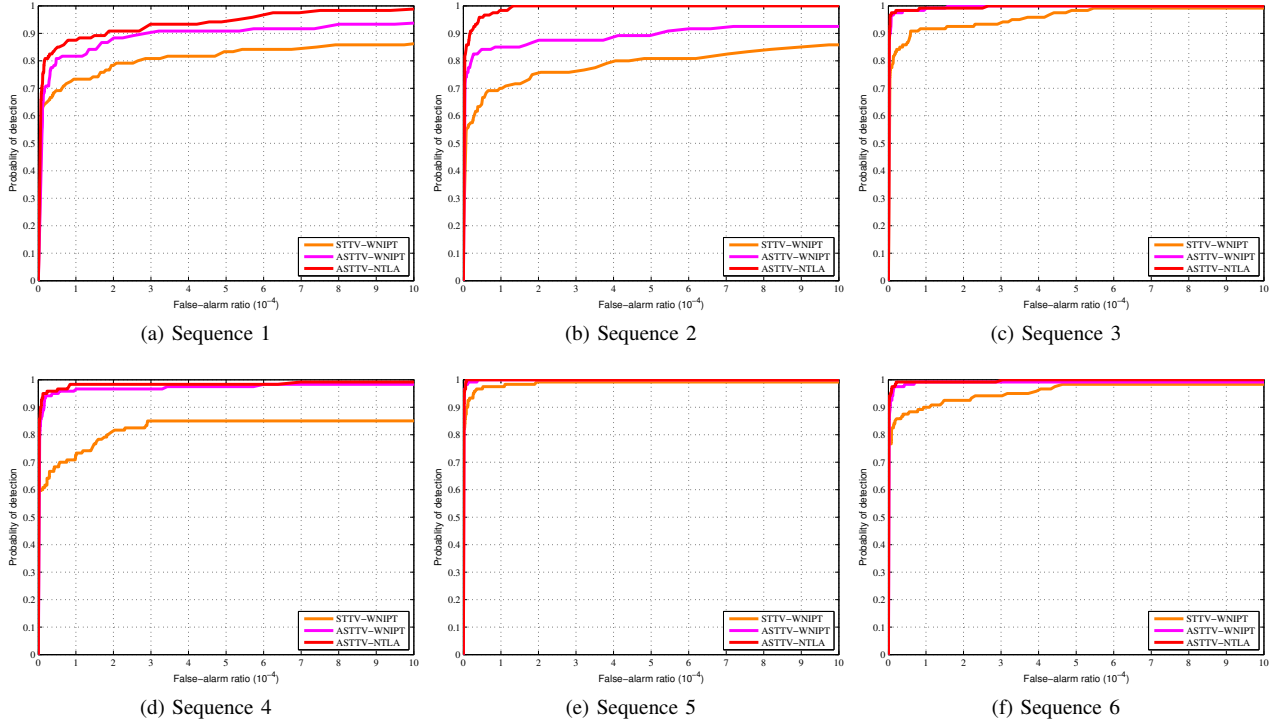


Figure 15. The ROC curves achieved by different variants of our method.

Table VI  
RUNNING TIME OF DIFFERENT METHODS

Methods	Sequence 1	Sequence 2	Sequence 3	Sequence 4	Sequence 5	Sequence 6
<b>Top-hat</b> [12]	32.52s	40.46s	33.79s	32.73s	32.42s	31.34s
<b>WSLCM</b> [18]	1087.39s	1701.05s	1411.60s	1450s	1451.99s	1400.41s
<b>TLLCM</b> [19]	282.67s	426.56s	363.79s	375.81s	370.85s	354.51s
<b>IPI</b> [22]	562.78s	841.23s	718.20s	772.45s	706.32s	745.97s
<b>NRAM</b> [26]	80.07s	223.71s	185.28s	153.01s	190.28s	157.94s
<b>TV-PCP</b> [31]	7976.50s	13314.75s	11144.09s	11339.91s	11164.87s	11233.05s
<b>SMSL</b> [29]	63.21s	74.90s	137.27s	72.91s	78.02s	71.92s
<b>RIPT</b> [4]	91.32s	153.93s	138.49s	112.31s	168.66s	131.04s
<b>PSTNN</b> [5]	29.97s	38.95s	34.86s	46.16s	52.04s	45.42s
<b>STTV-WNIPT</b> [8]	174.70s	293.81s	235.94s	243.41s	245.79s	245.77s
<b>ASTTV-NTLA (ours)</b>	206.64s	377.35s	287.89s	284.78s	280.17s	283.33s

but its performance is not good enough. In contrast, the speed of LRSD methods are relatively slow, because they need a lot of SVD operations. Among them, IPI and TV-PCP use accelerated proximal gradient (APG) method for optimization, and their execution time is relatively high. SMSL imposes constraints on the dictionary matrix but its efficiency cannot be guaranteed due to the APG solution. Other methods using ADMM framework are relatively more efficient, such as PSTNN, NRAM, RIPT, STTV-WNIPT and the proposed method. Among these methods, the speed of PSTNN is only slower than Top-hat. The main reason is that with the help of t-SVD and an additional stop condition, the complexity and computing time of the algorithm are dramatically reduced. For the last TV regularization based methods, the execution time of ASTTV-NTLA is much faster than that of the TV-PCP method with the help of the t-SVD and 3D FFT operation, but slightly slower than that of STTV-WNIPT. Considering the proposed method has achieved better performance in complex scenes, the sacrifice of computing time is acceptable.

## VI. CONCLUSION

To improve the ability of background suppression with complex scenes, an asymmetric spatial-temporal total variation regularized non-convex low-rank tensor approximation method was proposed. A Laplace function based surrogate for tensor rank is implemented to ensure adaptive weight assignment to all singular values, which helps reconstruct the background image more accurately. In addition, ASTTV regularization enables full utilization of the structural prior. Furthermore, ASTTV regularization term can effectively exploit both spatial and temporal information to detect the targets and suppress the background in non-smooth and non-uniform images. Extensive experimental results on synthetic and real infrared image demonstrate the promising detection performance of our method.

## VII. ACKNOWLEDGMENTS

This work was supported in part by the National Natural Science Foundation of China under Grant 61972435, Grant 61401474, and Grant 61921001.

## REFERENCES

- [1] S. Kim and J. Lee, "Scale invariant small target detection by optimizing signal-to-clutter ratio in heterogeneous background for infrared search and track," *Pattern Recognition*, vol. 45, no. 1, pp. 393–406, 2012.
- [2] Z. Liu, F. Zhou, X. Chen, X. Bai, and C. Sun, "Iterative infrared ship target segmentation based on multiple features," *Pattern Recognition*, vol. 47, no. 9, pp. 2839–2852, 2014.
- [3] X. Bai, Z. Chen, Y. Zhang, Z. Liu, and Y. Lu, "Infrared ship target segmentation based on spatial information improved fcm," *IEEE transactions on cybernetics*, vol. 46, no. 12, pp. 3259–3271, 2015.
- [4] Y. Dai and Y. Wu, "Reweighted infrared patch-tensor model with both nonlocal and local priors for single-frame small target detection," *IEEE journal of selected topics in applied earth observations and remote sensing*, vol. 10, no. 8, pp. 3752–3767, 2017.
- [5] L. Zhang and Z. Peng, "Infrared small target detection based on partial sum of the tensor nuclear norm," *Remote Sensing*, vol. 11, no. 4, p. 382, 2019.
- [6] Y. Sun, J. Yang, Y. Long, Z. Shang, and W. An, "Infrared patch-tensor model with weighted tensor nuclear norm for small target detection in a single frame," *IEEE Access*, vol. 6, pp. 76 140–76 152, 2018.
- [7] Y. Sun, J. Yang, Y. Long, and W. An, "Infrared small target detection via spatial-temporal total variation regularization and weighted tensor nuclear norm," *IEEE Access*, vol. 7, pp. 56 667–56 682, 2019.
- [8] Y. Sun, J. Yang, M. Li, and W. An, "Infrared small target detection via spatial-temporal infrared patch-tensor model and weighted Schatten p-norm minimization," *Infrared Physics & Technology*, vol. 102, p. 103050, 2019.
- [9] Y. Sun, J. Yang, and W. An, "Infrared dim and small target detection via multiple subspace learning and spatial-temporal patch-tensor model," *IEEE Transactions on Geoscience and Remote Sensing*, 2020.
- [10] X. Kong, C. Yang, S. Cao, C. Li, and Z. Peng, "Infrared small target detection via nonconvex tensor fibered rank approximation," *IEEE Transactions on Geoscience and Remote Sensing*, 2021.
- [11] M. M. Hadhoud and D. W. Thomas, "The two-dimensional adaptive lms (tdlms) algorithm," *IEEE Transactions on Circuits and Systems*, vol. 35, no. 5, pp. 485–494, 1988.
- [12] J.-F. Rivest and R. Fortin, "Detection of dim targets in digital infrared imagery by morphological image processing," *Optical Engineering*, vol. 35, no. 7, pp. 1886–1893, 1996.
- [13] S. D. Deshpande, M. H. Er, R. Venkateswarlu, and P. Chan, "Max-mean and max-median filters for detection of small targets," in *Signal and Data Processing of Small Targets 1999*, vol. 3809. International Society for Optics and Photonics, 1999, pp. 74–83.
- [14] S. Kim, Y. Yang, J. Lee, and Y. Park, "Small target detection utilizing robust methods of the human visual system for first," *Journal of Infrared, Millimeter, and Terahertz Waves*, vol. 30, no. 9, pp. 994–1011, 2009.
- [15] C. P. Chen, H. Li, Y. Wei, T. Xia, and Y. Y. Tang, "A local contrast method for small infrared target detection," *IEEE Transactions on Geoscience and Remote Sensing*, vol. 52, no. 1, pp. 574–581, 2013.
- [16] J. Han, Y. Ma, B. Zhou, F. Fan, K. Liang, and Y. Fang, "A robust infrared small target detection algorithm based on human visual system," *IEEE Geoscience and Remote Sensing Letters*, vol. 11, no. 12, pp. 2168–2172, 2014.
- [17] J. Han, K. Liang, B. Zhou, X. Zhu, J. Zhao, and L. Zhao, "Infrared small target detection utilizing the multiscale relative local contrast measure," *IEEE Geoscience and Remote Sensing Letters*, vol. 15, no. 4, pp. 612–616, 2018.
- [18] J. Han, S. Moradi, I. Faramarzi, H. Zhang, Q. Zhao, X. Zhang, and N. Li, "Infrared small target detection based on the weighted strengthened local contrast measure," *IEEE Geoscience and Remote Sensing Letters*, 2020.
- [19] J. Han, S. Moradi, I. Faramarzi, C. Liu, H. Zhang, and Q. Zhao, "A local contrast method for infrared small-target detection utilizing a tri-layer window," *IEEE Geoscience and Remote Sensing Letters*, vol. 17, no. 10, pp. 1822–1826, 2019.
- [20] X. Guan, Z. Peng, S. Huang, and Y. Chen, "Gaussian scale-space enhanced local contrast measure for small infrared target detection," *IEEE Geoscience and Remote Sensing Letters*, vol. 17, no. 2, pp. 327–331, 2019.
- [21] G. Liu, Z. Lin, S. Yan, J. Sun, Y. Yu, and Y. Ma, "Robust recovery of subspace structures by low-rank representation," *IEEE transactions on pattern analysis and machine intelligence*, vol. 35, no. 1, pp. 171–184, 2012.
- [22] C. Gao, D. Meng, Y. Yang, Y. Wang, X. Zhou, and A. G. Hauptmann, "Infrared patch-image model for small target detection in a single image," *IEEE Transactions on Image Processing*, vol. 22, no. 12, pp. 4996–5009, 2013.
- [23] E. J. Candès, X. Li, Y. Ma, and J. Wright, "Robust principal component analysis?" *Journal of the ACM (JACM)*, vol. 58, no. 3, pp. 1–37, 2011.
- [24] Y. Dai, Y. Wu, and Y. Song, "Infrared small target and background separation via column-wise weighted robust principal component analysis," *Infrared Physics & Technology*, vol. 77, pp. 421–430, 2016.
- [25] J. Guo, Y. Wu, and Y. Dai, "Small target detection based on reweighted infrared patch-image model," *IET Image Processing*, vol. 12, no. 1, pp. 70–79, 2017.
- [26] L. Zhang, L. Peng, T. Zhang, S. Cao, and Z. Peng, "Infrared small target detection via non-convex rank approximation minimization joint l2, l1 norm," *Remote Sensing*, vol. 10, no. 11, p. 1821, 2018.
- [27] T. Zhang, H. Wu, Y. Liu, L. Peng, C. Yang, and Z. Peng, "Infrared small target detection based on non-convex optimization with lp-norm constraint," *Remote Sensing*, vol. 11, no. 5, p. 559, 2019.
- [28] Y. He, M. Li, J. Zhang, and Q. An, "Small infrared target detection based on low-rank and sparse representation," *Infrared Physics & Technology*, vol. 68, pp. 98–109, 2015.
- [29] X. Wang, Z. Peng, D. Kong, and Y. He, "Infrared dim and small target detection based on stable multisubspace learning in heterogeneous scene," *IEEE Transactions on Geoscience and Remote Sensing*, vol. 55, no. 10, pp. 5481–5493, 2017.
- [30] T. Zhang, Z. Peng, H. Wu, Y. He, C. Li, and C. Yang, "Infrared small target detection via self-regularized weighted sparse model," *Neurocomputing*, vol. 420, pp. 124–148, 2021.
- [31] X. Wang, Z. Peng, D. Kong, P. Zhang, and Y. He, "Infrared dim target detection based on total variation regularization and principal component pursuit," *Image and Vision Computing*, vol. 63, pp. 1–9, 2017.
- [32] Z. Fan, D. Bi, L. Xiong, S. Ma, L. He, and W. Ding, "Dim infrared image enhancement based on convolutional neural network," *Neurocomputing*, vol. 272, pp. 396–404, 2018.
- [33] J. Ryu and S. Kim, "Small infrared target detection by data-driven proposal and deep learning-based classification," in *Infrared Technology and Applications XLIV*, vol. 10624. International Society for Optics and Photonics, 2018, p. 106241J.
- [34] B. Zhao, C. Wang, Q. Fu, and Z. Han, "A novel pattern for infrared small target detection with generative adversarial network," *IEEE Transactions on Geoscience and Remote Sensing*, 2020.
- [35] Y. Dai, Y. Wu, F. Zhou, and K. Barnard, "Asymmetric contextual modulation for infrared small target detection," in *Proceedings of the IEEE/CVF Winter Conference on Applications of Computer Vision*, 2021, pp. 950–959.
- [36] W. Hu, Y. Yang, W. Zhang, and Y. Xie, "Moving object detection using tensor-based low-rank and saliently fused-sparse decomposition," *IEEE Transactions on Image Processing*, vol. 26, no. 2, pp. 724–737, 2016.
- [37] Z. Zhang, G. Ely, S. Aeron, N. Hao, and M. Kilmer, "Novel methods for multilinear data completion and de-noising based on tensor-svd," in *Proceedings of the IEEE conference on computer vision and pattern recognition*, 2014, pp. 3842–3849.
- [38] M. Yuan and C.-H. Zhang, "On tensor completion via nuclear norm minimization," *Foundations of Computational Mathematics*, vol. 16, no. 4, pp. 1031–1068, 2016.
- [39] W. Hu, D. Tao, W. Zhang, Y. Xie, and Y. Yang, "The twist tensor nuclear norm for video completion," *IEEE transactions on neural networks and learning systems*, vol. 28, no. 12, pp. 2961–2973, 2016.
- [40] L. Chen, Y. Liu, and C. Zhu, "Iterative block tensor singular value thresholding for extraction of lowrank component of image data," in *2017 IEEE International Conference on Acoustics, Speech and Signal Processing (ICASSP)*. IEEE, 2017, pp. 1862–1866.
- [41] C. D. Martin, R. Shafer, and B. LaRue, "An order-p tensor factorization with applications in imaging," *SIAM Journal on Scientific Computing*, vol. 35, no. 1, pp. A474–A490, 2013.
- [42] M. E. Kilmer, K. Braman, N. Hao, and R. C. Hoover, "Third-order tensors as operators on matrices: A theoretical and computational framework with applications in imaging," *SIAM Journal on Matrix Analysis and Applications*, vol. 34, no. 1, pp. 148–172, 2013.
- [43] C. Lu, J. Feng, Y. Chen, W. Liu, Z. h. Lin, and S. Yan, "Tensor robust principal component analysis: Exact recovery of corrupted low-rank tensors via convex optimization," in *Proceedings of the IEEE conference on computer vision and pattern recognition*, 2016, pp. 5249–5257.
- [44] W.-H. Xu, X.-L. Zhao, T.-Y. Ji, J.-Q. Miao, T.-H. Ma, S. Wang, and T.-Z. Huang, "Laplace function based nonconvex surrogate for low-rank tensor completion," *Signal Processing: Image Communication*, vol. 73, pp. 62–69, 2019.
- [45] Y. Sun, J. Yang, and W. An, "Infrared small target detection based on reweighted infrared patch-image model and total variation regularization," in *Image and Signal Processing for Remote Sensing XXV*,

vol. 11155. International Society for Optics and Photonics, 2019, p. 111551F.

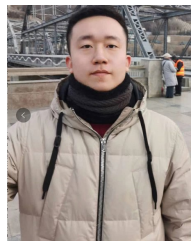
- [46] H. Fang, M. Chen, X. Liu, and S. Yao, "Infrared small target detection with total variation and reweighted regularization," *Mathematical Problems in Engineering*, vol. 2020, 2020.
- [47] L. Sun, T. Zhan, Z. Wu, and B. Jeon, "A novel 3d anisotropic total variation regularized low rank method for hyperspectral image mixed denoising," *ISPRS International Journal of Geo-Information*, vol. 7, no. 10, p. 412, 2018.
- [48] A. J. Tom and S. N. George, "Simultaneous reconstruction and moving object detection from compressive sampled surveillance videos," *IEEE Transactions on Image Processing*, vol. 29, pp. 7590–7602, 2020.
- [49] S. Boyd, N. Parikh, and E. Chu, *Distributed optimization and statistical learning via the alternating direction method of multipliers*. Now Publishers Inc, 2011.
- [50] Z. Lin, M. Chen, and Y. Ma, "The augmented lagrange multiplier method for exact recovery of corrupted low-rank matrices," *arXiv preprint arXiv:1009.5055*, 2010.
- [51] A. Beck and M. Teboulle, "A fast iterative shrinkage-thresholding algorithm for linear inverse problems," *SIAM journal on imaging sciences*, vol. 2, no. 1, pp. 183–202, 2009.
- [52] C. Gao, T. Zhang, and Q. Li, "Small infrared target detection using sparse ring representation," *IEEE Aerospace and Electronic Systems Magazine*, vol. 27, no. 3, pp. 21–30, 2012.
- [53] C. Gao, L. Wang, Y. Xiao, Q. Zhao, and D. Meng, "Infrared small-dim target detection based on markov random field guided noise modeling," *Pattern Recognition*, vol. 76, pp. 463–475, 2018.
- [54] C. Lu, J. Feng, Y. Chen, W. Liu, Z. Lin, and S. Yan, "Tensor robust principal component analysis with a new tensor nuclear norm," *IEEE transactions on pattern analysis and machine intelligence*, vol. 42, no. 4, pp. 925–938, 2019.
- [55] Y. Wang, J. Peng, Q. Zhao, Y. Leung, X.-L. Zhao, and D. Meng, "Hyperspectral image restoration via total variation regularized low-rank tensor decomposition," *IEEE Journal of Selected Topics in Applied Earth Observations and Remote Sensing*, vol. 11, no. 4, pp. 1227–1243, 2017.



**Ting Liu** received the B.E. degree in electrical engineering and automation from Hunan Institute of Engineering, Xiangtan, China, in 2017, and the M.E. degree in control engineering from Xiangtan University (XTU), Xiangtan, China, in 2020. She is currently pursuing the Ph.D. degree with the College of Electronic Science in NUDT, Changsha, China. Her research interests focus on signal processing, target detection and image processing.



**Jungang Yang** received the B.E. and Ph.D. degrees from National University of Defense Technology (NUDT), in 2007 and 2013 respectively. He was a visiting Ph.D. student with the University of Edinburgh, Edinburgh from 2011 to 2012. He is currently an associate professor with the College of Electronic Science, NUDT. His research interests include computational imaging, image processing, compressive sensing and sparse representation. Dr. Yang received the New Scholar Award of Chinese Ministry of Education in 2012, the Youth Innovation Award and the Youth Outstanding Talent of NUDT in 2016.



detection and deep learning.

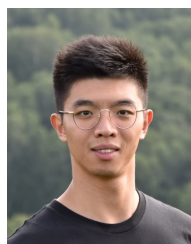


**Boyang Li** received the B.E. degree in Mechanical Design manufacture and Automation from the Tianjin University, China, in 2017 and M.S. degree in biomedical engineering from National Innovation Institute of Defense Technology, Academy of Military Sciences, Beijing, China, in 2020. He is currently working toward the PhD degree in information and communication engineering from National University of Defense Technology (NUDT), Changsha, China. His research interests focus on VHR remote sensing image classification, infrared small target

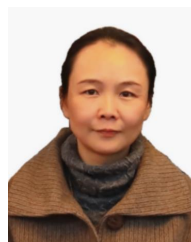
**Chao Xiao** received the BE degree in the communication engineering and the ME degree in information and communication engineering from the National University of Defense Technology (NUDT), Changsha, China in 2016 and 2018, respectively. He is currently working toward the Ph.D. degree with the College of Electronic Science in NUDT, Changsha, China. His research interests include deep learning, small object detection and object tracking.



**Yang Sun** received the Ph.D. degree in information and communication engineering from the National University of Defense Technology (NUDT), Changsha, China, in 2020. He is currently a postdoctoral with the College of Electronic Science, NUDT. His research interests are image processing and infrared target detection..



**Yingqian Wang** received the B.E. degree in electrical engineering from Shandong University (SDU), Jinan, China, in 2016, and the M.E. degree in information and communication engineering from National University of Defense Technology (NUDT), Changsha, China, in 2018. He is currently pursuing the Ph.D. degree with the College of Electronic Science and Technology, NUDT. His research interests focus on low-level vision, particularly on light field imaging and image super-resolution.



**Wei An** received the Ph.D. degree from the National University of Defense Technology (NUDT), Changsha, China, in 1999. She was a Senior Visiting Scholar with the University of Southampton, Southampton, U.K., in 2016. She is currently a Professor with the College of Electronic Science and Technology, NUDT. She has authored or co-authored over 100 journal and conference publications. Her current research interests include signal processing and image processing.